ChemElectroChem

Review
doi.org/10.1002/celc.202300646

Chemistry Europe
European Chemical Societies Publishing

www.chemelectrochem.org

Porous Transport Photoelectrodes Fabricated on Felt Substrates and Applications to Polymer Electrolyte Photoelectrochemistry

Fumiaki Amano,*[a] Rizki Marcony Surya,[a] and Surya Pratap Singh[a]

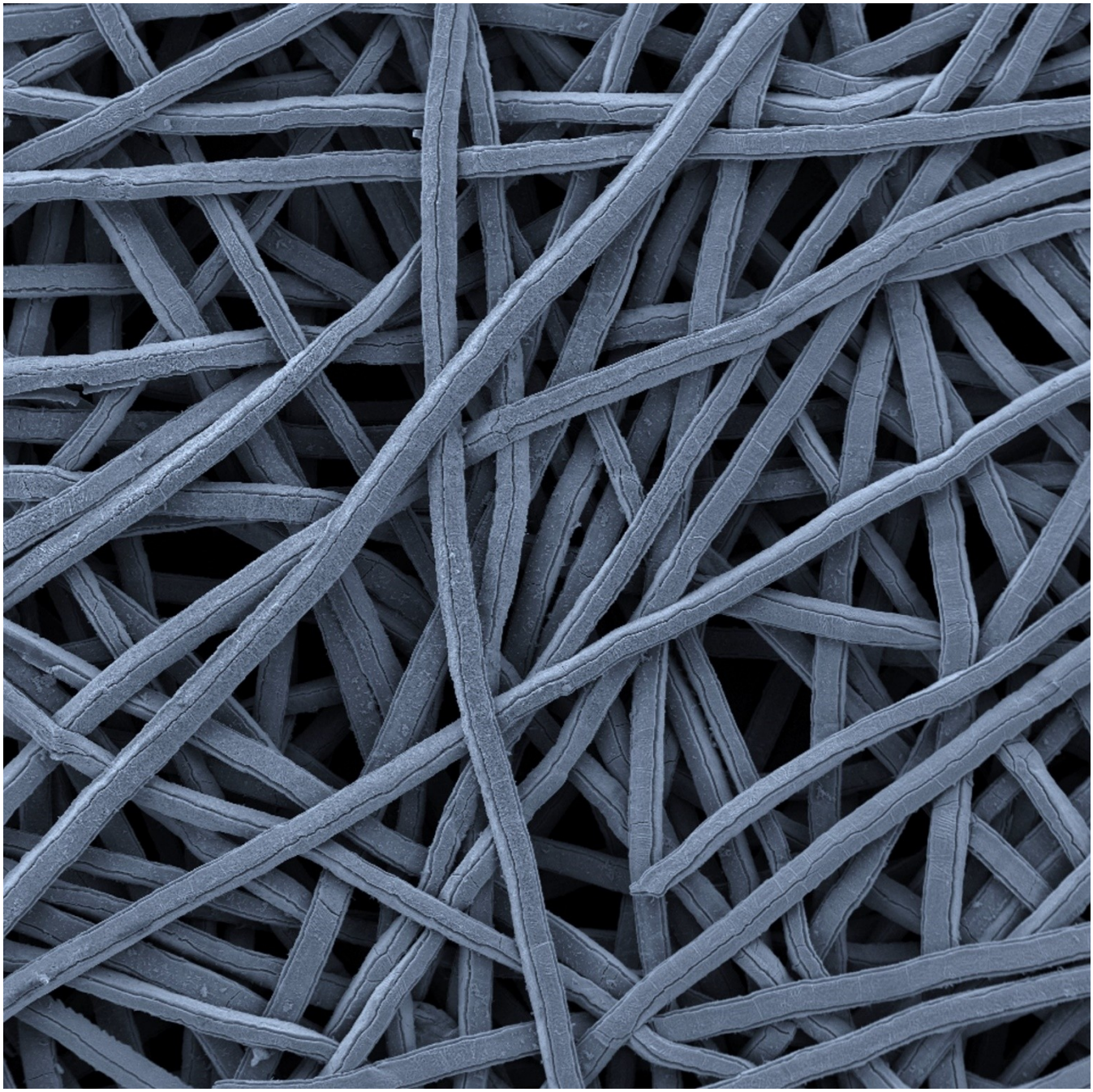

Photoelectrochemistry is used to develop solar energy technologies for fuel production and chemical transformations. Semiconductor materials such as TiO_2, WO_3, $BiVO_4$, Fe_2O_3, and Cu_2O are often investigated in devices designed to convert light energy into chemical energy, including for the production of hydrogen by photoelectrochemical (PEC) water splitting. The oxide electrodes are of significant interest due to their potential for efficient PEC reactions with high durability and their relatively low costs compared to other semiconductor materials. This review highlights the roles played by macroporous photoelectrodes in the development of highly efficient photoelectrodes and advanced PEC systems using polymer electrolytes. Three-dimensional conductive fiber substrates, such as titanium felt and carbon paper, outperform their two-dimensional counterparts owing to their larger interfacial areas that enhance PEC properties. The macroporous structures facilitate mass-transport-limited reactions when integrated with polymer electrolytes in membrane electrode assemblies. Such configurations are promising for PEC splitting of pure water, and for transforming gaseous molecules such as water vapor, volatile organic compounds, and methane. Optimizing the configuration, including electrode materials selection and ionomer-coating treatment, can potentially improve the performance of polymer electrolyte membrane PEC cells. Porous transport photoelectrodes integrated with proton/anion-exchange membranes offer significant opportunities for advanced PEC applications.

1. Introduction

Photochemistry involves light harvesting, energy conversion, and storage in the form of chemical energy. Because sunlight is a limitless global energy source, the practical conversion of solar energy has been extensively investigated to fulfill the high demands for energy over the past several decades. A system that uses a rutile TiO_2 photoanode was first introduced for the photoelectrochemical (PEC) process by Fujishima and Honda in 1972.[1] Light energy is captured to convert water into molecular hydrogen and oxygen using photoactive semiconductors in aqueous-based electrolytes. The evolution of H_2 and O_2 from water has a standard free energy (ΔG°) of 237.2 kJ mol^{-1}, which corresponds to a cell voltage (E°_{cell}) of 1.23 V. A schematic diagram of a PEC water-splitting system using a photoanode is presented in Figure 1A.[2] The photoanode promotes the oxygen-evolution reaction (OER, $2H_2O \rightarrow O_2 + 4H^+ + 4e^-$) and the cathode promotes the hydrogen-evolution reaction (HER, $2H^+ + 2e^- \rightarrow H_2$). When an n-type semiconductor is exposed to light of energy higher than its bandgap, photoexcitation occurs through the absorption of light, and the photogenerated holes in the valence band (VB) promote water oxidation for the OER. The remaining electrons in the conduction band (CB) move to the cathode as a photocurrent. Band positions close to the flat band lead to photogenerated electron-hole recombination at a low applied potential. Conversely, band bending occurs in n-type semiconductors at an applied potential that is more positive than the flat-band potential (Figure 1B). The electric field within the semiconductor (space charge layer) enhances charge separation and charge-transfer reactions at the semiconductor surface. The applied bias voltage enhances not only the photoanodic OER but also the cathodic HER. In contrast to a photocatalytic powder system, pure hydrogen is easily obtained in a PEC system when a membrane is used to separate the gas-evolution electrodes. Therefore, the reverse reaction that forms water from hydrogen and oxygen is also inhibited in a membrane-separated two-compartment PEC cell.

The low PEC efficiency associated with photoexcited electron-hole recombination is the most serious drawback of oxide photoelectrodes, such as Fe_2O_3, WO_3, and $BiVO_4$. Increasing the crystallinity can be one of the efficient ways to decrease the recombination. The surface layer and co-catalyst loading should also be selected to enhance PEC performance (Figure 1C).[3] The surface coating acts as a passivation or p-n junction layer that decreases recombination at surface states and protects against (photo)chemical corrosion. The co-catalyst on the photoanode contributes to facile hole transfer from the VB to the electrolyte interface by decreasing the reaction overpotential for the O_2-evolving oxidation of water. The enhanced surface reaction kinetics results in less recombination and higher photocurrent density (J_{photo}). A lower overpotential leads to a negative shift of the photocurrent onset potential in the photoanodic reaction (Figure 1D). Additionally, controlling the semiconductor morphology and nanostructure can improve the J_{photo} by shortening the distance traveled by minority carriers from the light-absorption site to the surface. Combining these treatment methods can lead to an ideal photoanode with a high J_{photo} and a negative onset potential.

Furthermore, the choice of semiconductor used as the photoabsorber also needs to be considered (Figure 1E). The bandgap determines the ability of a photoelectrode to harvest light. Consequently, narrow-bandgap semiconductors, which are capable of absorbing an enormous amount of visible light from solar energy, are required. Oxide-based n-type semiconductors are more (photo)stable during the OER and are attractive in terms of their manufacturing costs compared with Si and group III–V semiconductors. Some metal oxides possess suitable bandgap energies needed to utilize the UV and visible-light spectrum (1.5–3.2 eV for 390–830 nm). The positions of the CB and VB edges are also important for promoting the HER and OER, respectively. The VB edge of the OER photoanode should be more positive than the thermodynamic potential (i.e., 1.23 V

[a] Prof. F. Amano, R. M. Surya, Dr. S. P. Singh
Department of Applied Chemistry for Environment
Tokyo Metropolitan University
1-1 Minami-Osawa, Hachioji, Tokyo 192-0397, Japan
E-mail: f.amano@tmu.ac.jp
Homepage: https://amanolab.cpark.tmu.ac.jp/amanolab/ja/index.html

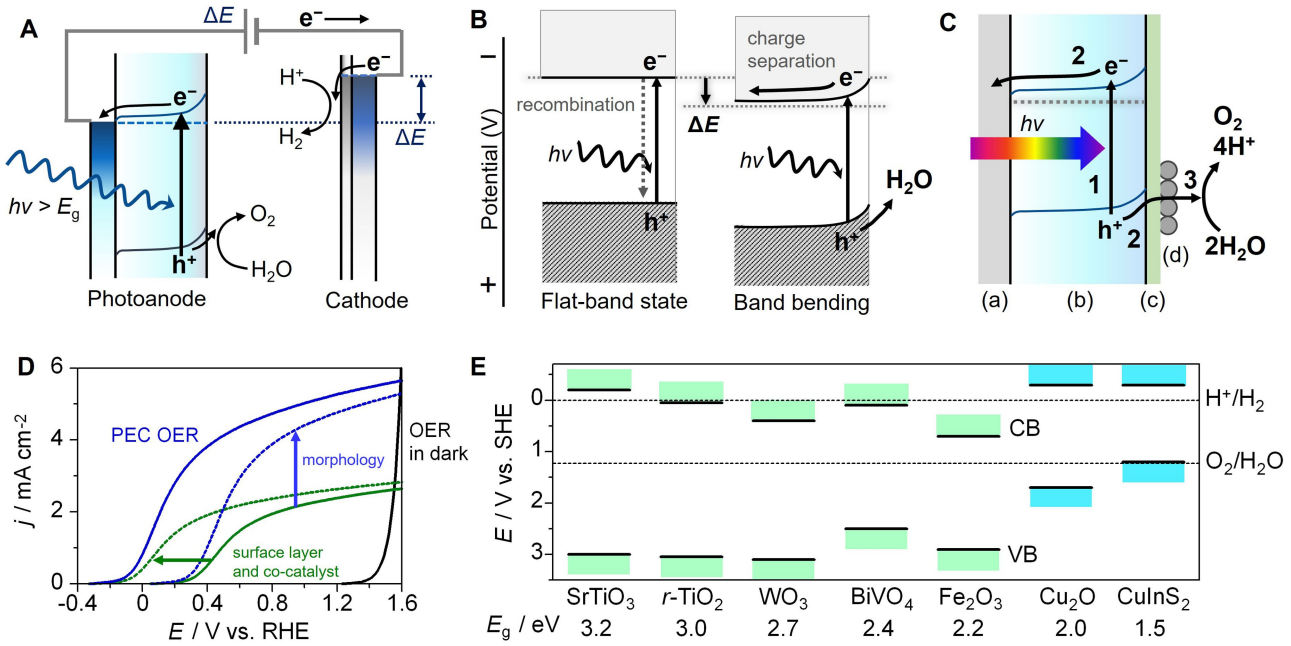

Figure 1. (A) Schematic illustration of PEC water splitting using a photoanode for OER and a cathode for HER with applied bias voltage (ΔE). (B) Band diagram of an n-type semiconductor electrode photoirradiated at various applied potentials. (C) Effect of the surface layer, which suppresses electron-hole recombination, and the OER co-catalyst, which facilitates hole transfer to water (a: substrate, b: semiconductor, c: surface layer, d: co-catalyst). (D) Comparing typical PEC photoanode performance using surface-layer, co-catalyst-loading, and morphology-control strategies. (E) Band alignments of several semiconductor materials for the water-splitting reaction (*r*-TiO_2: rutile, CB: conduction band, VB: valence band, green: n-type semiconductor, blue: p-type semiconductor). Adapted from Ref. [2]. Copyright (2021), with permission from Wiley-VCH.

vs. the reversible hydrogen electrode (RHE)). Similarly, the CB edge of the photocathode should be more negative than the HER potential (i.e., 0 V vs. RHE). The Fermi level, which is identical to the flat-band potential, is located just below the CB edge for an n-type semiconductor and above the VB edge for a p-type semiconductor; the flat-band potential affects the applied potential required for band bending.

Surface modification and co-catalyst loading are well-known methods for enhancing the PEC performance of a semiconductor material. However, the effect of the substrate structure has not been elaborated. Herein, we present an overview of recent developments in macroporous photoelectrodes with three-dimensional (3D) fiber structures for use in photoelectrochemical applications. A strategy that employs 3D porous substrates has led to higher PEC performance compared

Prof. F. Amano received his Ph.D. from Kyoto University (working with Prof. T. Tanaka) in 2006. He joined Prof. B. Ohtani's group as an assistant professor at Hokkaido University in 2006. He moved to the University of Kitakyushu in 2011. Since 2022, he has been a professor at Tokyo Metropolitan University (TMU). His research interests include photocatalysis, photoelectrochemistry, and electrocatalysis.

Rizki Marcony Surya received his Bachelor of Chemistry from Universitas Indonesia in 2020. He joined Professor Amano's laboratory at TMU in 2022 as an M.Sc. student. He has recently been studying macroporous Cu_2O photocathodes for solar fuel production.

Surya Pratap Singh completed his M.Sc. in Chemistry at the Indian Institute of Technology Hyderabad in 2018. He then moved to Japan and obtained his Ph.D. from Kyoto University in 2022 under the supervision of Prof. H. Yoshida. He is currently a postdoctoral research fellow at TMU. His research interests include photocatalytic and photoelectrochemical methane conversion.

to that of conventional two-dimensional (2D) substrates. The porous structures facilitate gas diffusion and ion transport. In addition, we introduce a PEC system that uses a membrane electrode assembly composed of a gas-diffusion photoelectrode and a porous transport photoelectrode with a polymer electrolyte membrane. The potential performances of several PEC applications are discussed.

2. Macroporous photoelectrodes

2.1. Microfiber-felt substrates

Porous conductive substrates have attracted considerable attention for the preparation of photoelectrodes. Macroporous felts with 3D interconnected fibrous structures have been extensively used as porous substrates. The specific surface area of a Ti-felt substrate (444 $cm^2 g^{-1}$) is higher than that of a flat Ti-sheet substrate (45 $cm^2 g^{-1}$) at the same thickness.[4] Figure 2A compares dense 2D and fibrous 3D substrates; assuming the same volume: a dense rectangular (4×4×8 cm) substrate has a surface area of 160 cm^2, while 16 fibers of 8 cm length have a surface area of 544 cm^2. This property endows the conductive substrate with a larger interface, resulting in the formation of thin semiconductor layers at similar loadings (Figure 2B), thereby shortening the distance traveled by photogenerated carriers and improving PEC efficiency. A 3D conductive substrate with a large surface area provides a large semiconductor surface, which is beneficial for enhancing photoabsorption while maintaining layer thickness.[5,6] Several porous photoanodes (n-type TiO_2, WO_3, $BiVO_4$, Fe_2O_3, and $SrTiO_3$) and photocathodes (p-type $CuInS_2$ and Cu_2O) have been prepared on porous felt substrates composed of carbon and titanium microfibers.[4–13] Carbon microfibers could be oxidatively decomposed during thermal treatments and photoanodic reactions. In contrast, titanium microfibers have better tolerance under oxidative conditions compared with carbon microfibers.

Porous conductive substrates (carbon paper and titanium felt) have been used as gas-diffusion layers and porous transport layers in fuel cells and water-electrolysis cells. The gas-diffusion structure of a 3D fibrous substrate is effective for mass-transport-limited reactions. Gas-phase PEC cells that use porous photoelectrodes with integrated polymer electrolyte membranes have been investigated for vapor-fed water splitting (Figure 2C).[4,14–17] The porous photoelectrode is attached to a proton-exchange membrane (PEM) and an anion-exchange membrane (AEM). Membrane photoelectrode assemblies have been successfully investigated for advanced PEC reactions without the use of liquid electrolytes. The photoelectrodes of a membrane-based cell should be porous for ion transport from the semiconductor surface to the membrane. Gas-phase reactions also require high porosities to enable gas to be fed to the electrode interface.

2.2. Photoanodes on felt substrates

2.2.1. TiO_2 on felt

Tsampas *et al.*[17,18] and Amano *et al.*,[7,9,19] separately reported the preparation of TiO_2 nanotube arrays (TNTAs) on 3D porous Ti-felt substrate by electrochemical anodization and subsequent annealing in air/O_2, as depicted in Figure 3A. Tsampas *et al.* conducted anodization at 30 V using the electrolyte (ethylene glycol containing 0.3 wt% ammonium fluoride and 2 vol% water) pre-aged with a dummy sample for 10 h to minimize cracks and the detachment of TNTA.[17,18] Nanotube length was dependent on anodization time (Figure 3B), with 700-nm-long nanotubes with 10–15 nm inner diameters obtained after anodization for 1 h. The TNTA had a BET specific surface area of 2.7 $m^2 g^{-1}$ and a total surface area that was 33-times higher after anodization compared to that of the untreated Ti felt. The PEC water-splitting activity was evaluated in 0.1 M aqueous H_2SO_4 (pH 1) under UV-LED at room temperature.

Figure 3C shows linear sweep voltammograms of anodized-TNTA and non-anodized TiO_2 samples annealed at different temperatures for 5 h in air.[18] The anatase phase was mainly observed for TNTAs annealed below 500 °C, and a rutile TiO_2 phase dominated the non-anodized TiO_2. Both photoanodes show photocurrent enhancements that correlate with the calcination temperature. The TNTA exhibited a J_{photo} that began to rise at ~0.1 V (vs. RHE), whereas the rutile layer required

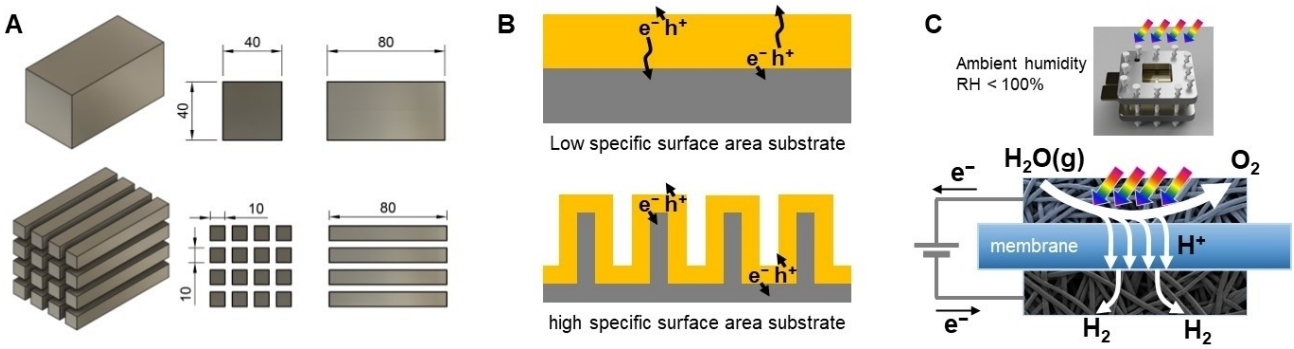

Figure 2. (A) Illustration of how the specific surface areas of a dense substrate and a fiber structure are determined. (B) Schematic illustration of the distances traveled by charge carriers in semiconductor layers coated on 2D and 3D conductive substrates with different specific surface areas. (C) Conceptual image of a gas-diffusion PEC cell using a porous photoelectrode and polymer electrolyte membrane for water splitting from humidity in the air.

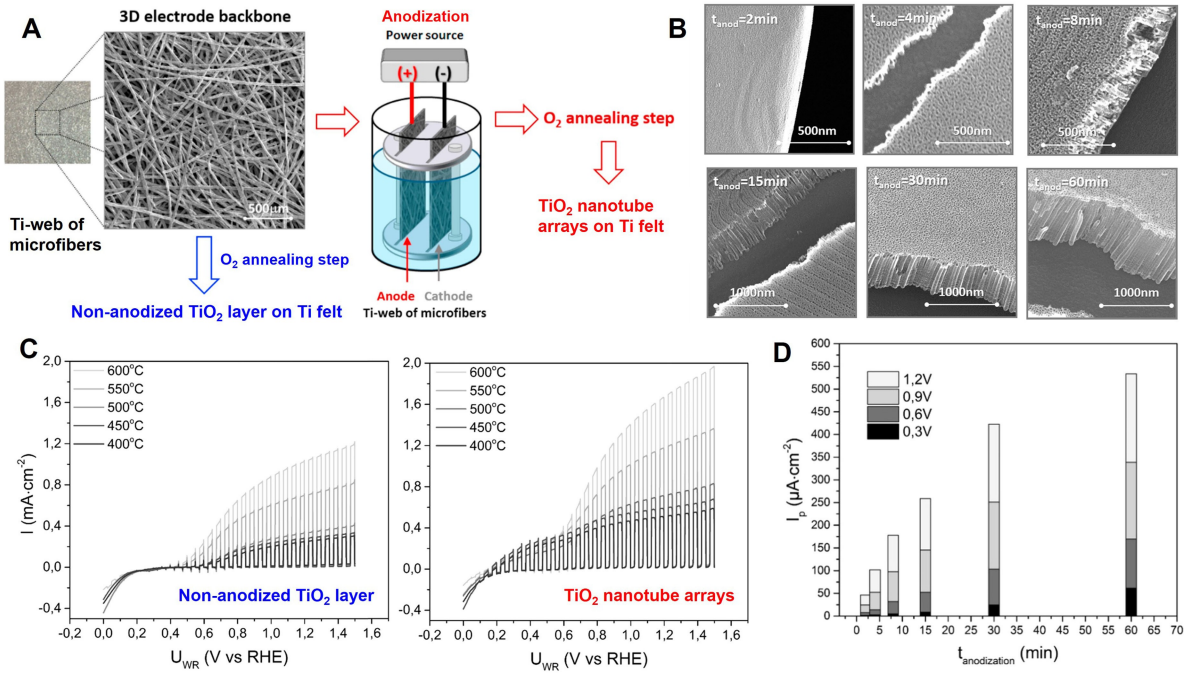

Figure 3. (A) Routes for the preparation of TiO_2 nanotube arrays (TNTAs) and a non-anodized TiO_2 layer on Ti felt. (B) SEM images of TNTAs prepared by anodization at 30 V for various anodization times (t_{anod} = 2–60 min). (C) Linear sweep voltammograms (2.5 mV s^{-1}) of non-anodized TiO_2 and TNTA (t_{anod} = 60 min) layers in 0.1 M H_2SO_4 (pH 1) under chopped UV illumination (365 nm, 9 mW cm^{-2}). The samples were annealed at different temperatures for 5 h in air. (D) Photocurrent densities at different applied potentials (V vs. RHE) as functions of t_{anod} for TNTAs annealed at 450 °C in air. Adapted from Ref. [18]. Copyright (2018), with permission from Elsevier.

higher onset potentials of 0.4–0.6 V. The voltammograms acquired for TNTA clearly show two plateaus at low (< 0.55 V) and high (> 0.55 V) potentials; the first is hardly dependent on calcination temperature, whereas the second increases with increasing calcination temperature. The TNTAs/Ti-felt calcined at 600 °C showed the highest J_{photo} at 1.2 V (vs. RHE). Further post-treatment was reported for a TNTAs/Ti-plate annealed in air at 650 °C; the second treatment was performed under flowing nitrogen at higher temperatures (750–850 °C), which led to a higher J_{photo} despite the anatase nanotube structure transforming into rutile TiO_2 particles.[20] Figure 3D shows how anodization time affects J_{photo} in each voltammogram. A longer anodization time results in longer tubes and a greater J_{photo}. Tsampas *et al.* used a porous TNTA photoanode in a gas-phase PEM-PEC cell; however, this cell was operated at greater than 100% relative humidity (RH) in the presence of liquid condensation, which are not real gas-phase conditions.[17,18]

TNTAs were also prepared on Ti felt by anodization in ethylene glycol containing 0.25 wt% ammonium fluoride and 10 vol% H_2O at 50 V for 3 h, followed by annealing in air at 550 °C for 1 h to facilitate anatase-phase crystallization of the amorphous nanotubes.[7] The nanotubes were 5 µm long, with inner pores 130–160 nm in size. TNTAs/Ti-felt exhibited an incident photon-to-current conversion efficiency (IPCE), which is defined as the ratio of the photocurrent to the incident-photon flux, of 26.5% at 365 nm (UV LED, 43 mW cm^{-2}) and 1.2 V vs. RHE in neutral aqueous solution (pH 6.7). The rutile TiO_2 layer on the Ti felt, which was thermally oxidized at 650 °C for 2 h, exhibited an IPCE of 17.5% at 365 nm and 1.2 V (vs. RHE).[21] A comparison of the 3D Ti felt and 2D Ti plate revealed that the porous TNTAs/Ti felt exhibited a higher IPCE than the flat TNTAs/Ti plate in both neutral and acidic solutions (nanotube length: 3 µm).[9] The reaction sites in the TNTAs were visualized by scanning electrochemical cell microscopy.[19] PEC-deposited PbO_2 particles revealed that reaction sites were located on the inner and outer surfaces of the tube walls, and depended on the wavelength, which affects the penetration depth of the light.[9]

Gas-phase PEC-performance data for TiO_2/Ti-felt photoanodes were reported at RH < 100%. The surface of the photoanode needs to be coated with a perfluorosulfonic acid (PFSA) ionomer for vapor-fed PEC water-splitting applications in the absence of liquid condensation.[7,21] A TNTAs/Ti-felt photoanode coated with the ionomer exhibited an IPCE of 21% under UV light (365 nm) in a PEM-PEC system, whereas the ionomer-coated rutile TiO_2 layer exhibited an IPCE of 16%. In contrast, rutile TiO_2 showed a much higher IPCE (11%) under violet light (385 nm) than the TNTAs (5.6%).[21] The higher activity exhibited by rutile TiO_2 at 385 nm is attributable to its narrower bandgap (3.0 eV) compared to that of anatase (3.2 eV).

2.2.2. WO_3 on felt

Tungsten trioxide (WO_3) is a visible-light-sensitive semiconductor with an indirect bandgap of approximately 2.6–2.7 eV and a photoabsorption edge located near the blue-light region. Abe *et al.* prepared porous WO_3 photoanodes using 3D-structured

carbon microfiber felt (CMF).[22,23] CMF is a conductive substrate used in fuel and water-electrolysis cells; however, their use as photoelectrode substrates is limited. The high porosity and large surface area provided by the interconnected fiber structure are advantageous for achieving highly porous semiconductor particles with few grain boundaries.

WO_3/CMF was prepared by simple impregnation of a water-soluble tungsten precursor (ammonium metatungstate, $(NH_4)_6H_2W_{12}O_{40}$) followed by calcination at 640 °C.[22,23] The hydrophobic CMF is pre-calcined in air at 640 °C to form a hydrophilic carbon surface for better impregnation. Polyethylene glycol 300 (PEG) was added to the precursor to improve its affinity for CMF. Figure 4A shows SEM images of CMF loaded with different amounts of WO_3 (6.7, 14, and 20 mg cm^{-2}). The use of the PEG additive enables fine WO_3 particles (~150 nm) to be preferentially loaded onto the carbon fiber surface rather than in the voids, which is probably due to the high viscosity resulting from the addition of PEG, which retains the precursor dispersion during the drying process. The density of WO_3 particles loaded onto the carbon fibers increased with increasing WO_3 loading. WO_3 particles also loaded into void spaces.

The PEC properties of the WO_3/CMF photoanodes were examined in 0.1 M Na_2SO_4 (pH 5.8) containing 2-propanol as a hole scavenger.[22,23] Figure 4B presents J_{photo} data at 1.1 V (vs. RHE) under visible-light irradiation (400–500 nm) as a function of WO_3 loading. For comparison, fluorine-doped tin oxide (FTO) glass was used as a conventional 2D conductive substrate. WO_3/FTO, which was prepared following a sol-gel procedure and calcination at 500 °C, exhibited a maximum J_{photo} at 1.2 mg cm^{-2}. The higher WO_3 content on the 2D substrate resulted in a dramatically lower J_{photo}, which is most likely due to the higher number of grain boundaries formed in the thick WO_3 layer. In contrast, the J_{photo} of WO_3/CMF increased to its highest value (2.2 mA cm^{-2}) as the WO_3 loading was increased to ~12 mg cm^{-2}, which suggests that the WO_3 particles loaded on the carbon fibers and those in the voids contribute to generating photocurrent at 1.1 V vs. RHE. However, direct electron injection from WO_3 into the carbon fiber is more likely to occur at lower applied potentials, rather than indirect injection through the grain boundaries in the aggregated WO_3 particles (Figure 4C). The optimized WO_3/CMF with its 3D porous structures exhibited a much higher J_{photo} than a conventional WO_3 photoanode on a 2D substrate.

Ti microfiber felt has also been used to prepare porous WO_3 photoanodes.[24] Figure 4D shows IPCE action spectra of various WO_3 photoanodes on different conductive substrates (Ti felt, Ti sheet, and FTO glass). The 3D WO_3/Ti-felt exhibited higher IPCE values than the 2D WO_3/Ti-sheet and WO_3/FTO in the UV and visible light regions, respectively, which is attributable to higher photoabsorption due to the larger amount of WO_3 loaded on the high-surface-area Ti felt. Figure 4E shows that the titanium substrate is more suitable for WO_3 photoanodes prepared at high temperatures than conventional transparent conductive oxides, such as FTO and indium tin oxide (ITO).[25] Porous Ti felt

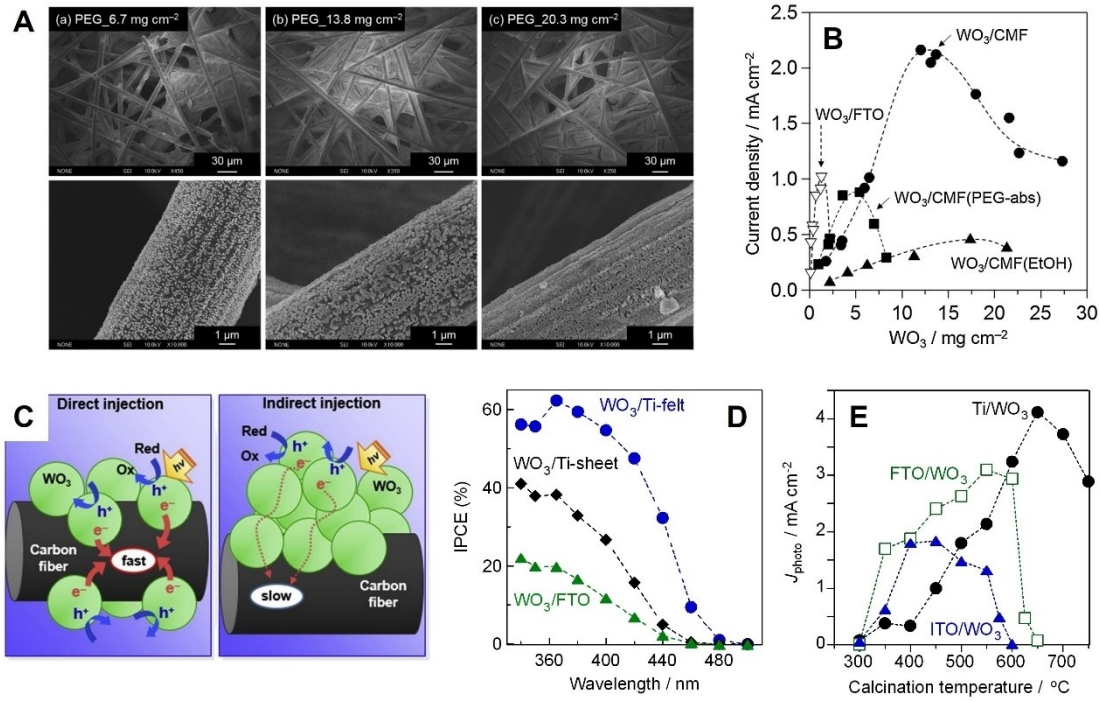

Figure 4. (A) SEM images of carbon microfiber felt (CMF) with various WO_3 loadings (6.7, 14, and 20 mg cm^{-2}) prepared from a PEG-added precursor.[23] (B) Photocurrent densities (J_{photo}) at 1.1 V (vs. RHE) for WO_3/CMF and WO_3/FTO samples in aqueous 0.1 M Na_2SO_4 containing 1.0 M 2-propanol (pH 5.8) under visible light as functions of WO_3 loading. WO_3/CMF(PEG-abs) was prepared by absorbing excess precursor solution to minimize WO_3 loading in voids. (C) Schematic illustration of direct electron injection from WO_3 particles to the carbon fiber and indirect injection through the thick WO_3 layer on the conductive substrate. (D) IPCE action spectra of WO_3 photoanodes prepared on various substrates (Ti felt, Ti sheet, and FTO glass) in 0.2 M Na_2SO_4 (pH 2.2) at 1.33 V (vs. RHE).[24] (E) J_{photo} values of WO_3 layers loaded on Ti sheet, FTO glass, and ITO glass as functions of calcination temperature in 0.1 M H_2SO_4 (pH 1.0) at 1.05 V (vs. RHE) under UV-visible irradiation.[25] Adapted from Ref. [23–25]. Copyright (2017, 2019, and 2022), with permission from Elsevier.

is a suitable substrate due to the large surface area and better oxidation durability than carbon felt.

2.2.3. $BiVO_4$ on felt

Bismuth vanadate ($BiVO_4$), with its monoclinic scheelite structure, is a visible-light-responsive semiconductor with a bandgap of approximately 2.4 eV. Constructing a $BiVO_4$ heterojunction with WO_3 is a favorable process because their bands are appropriately aligned, which enhances charge-separation efficiency.[26] Porous $BiVO_4$ photoanodes have been extensively investigated because they are potentially applicable as gas-diffusion electrodes in polymer-electrolyte photoelectrochemistry.[11,14,15]

Tsampas *et al.* prepared $WO_3/BiVO_4$ photoanodes on 3D Ti microfibers as porous-photoanode scaffolds.[14] The $BiVO_4$ layer was deposited using the successive ionic-layer adsorption and reaction (SILAR) method with 0.05 M $Bi(NO_3)_3$ and 0.05 M NH_4VO_3 precursor solutions (Figure 5A). The SILAR cycle included dip coating alternating layers (1 min) with rinse steps in between. Figure 5B shows the surface morphologies of the WO_3 and $WO_3/BiVO_4$ layers on Ti-felt substrates. The WO_3 layer was formed by anodizing (30 V for 2 min) a 200 nm-thick tungsten film deposited on Ti felt by DC magnetron sputtering with subsequent calcination at 500 °C for 1 h. The $WO_3/BiVO_4$ heterojunction was prepared through 40 SILAR cycles, calcination (550 °C for 1 h), and etching in 1 M KOH to remove undesired V_2O_5. The $BiVO_4$ particles (~180 nm) were well-distributed, with a few agglomerates on the low-roughness WO_3 layer. Figure 5C shows that the $WO_3/BiVO_4$ heterojunction exhibited a J_{photo} value of up to 2.3 mA cm^{-2} under visible light (> 395 nm, 100 mW cm^{-2}) in 0.1 M H_2SO_4 (pH 1.0), while WO_3 and $BiVO_4$ alone delivered low currents (0.10 and 0.25 mA cm^{-2}, respectively). The porous $WO_3/BiVO_4$ photoanode was used in a "gas-phase" PEM-PEC reaction (RH > 100 %).[14] However, the necessity of surface-functionalizing porous photoanodes with PFSA ionomers was recently reported for gas-phase PEM-PEC cells (RH < 100 %).[11,27] In the absence of the WO_3 layer, 3 % tungsten-doped $BiVO_4$/Ti-felt also exhibited a high J_{photo} value (2.1 mA cm^{-2}) at 1.23 V vs. RHE in 0.1 M aqueous sodium phosphate (NaPi) (pH 6.0) under 1-sun illumination (AM1.5G, 100 mW cm^{-2}).[11]

Amano *et al.* also prepared porous WO_3/Mo-doped $BiVO_4$ on Ti felt using a simple dip-coating method.[15] Figure 5D shows the PEC properties of porous $BiVO_4$-based photoanodes when illuminated by visible light in 0.1 M NaPi. Doping Mo^{5+} into $BiVO_4$ led to a significantly higher J_{photo} value at 1.2 V (vs. RHE) under blue light (454 nm); Ti/$BiVO_4$, Ti/WO_3, Ti/WO_3/$BiVO_4$, and Ti/WO_3/Mo-$BiVO_4$ exhibited IPCE efficiencies of 0.8, 3.2, 4.4, and 10.7 %, respectively. The influence of higher-valence-cation (Mo^{5+} and W^{6+}) doping is explained by enhanced n-type conductivity in bulk $BiVO_4$. The IPCE action spectra show that Ti/WO_3/Mo-$BiVO_4$ exhibits the highest IPCE value at 480 nm, with an onset wavelength of 500 nm. Porous Ti/WO_3/Mo-$BiVO_4$ exhibited superior PEC performance than 2D FTO/WO_3/Mo-$BiVO_4$.[28]

2.2.4. $SrTiO_3$ on felt

Strontium titanate ($SrTiO_3$), with a bandgap energy of 3.2 eV, is a suitable photocatalyst for overall water splitting. $SrTiO_3$ evolves H_2 and O_2 in a 2 : 1 stoichiometric ratio, and its quantum efficiency has been improved by up to 96 % in the 350–360 nm wavelength region through Al doping and selective photo-

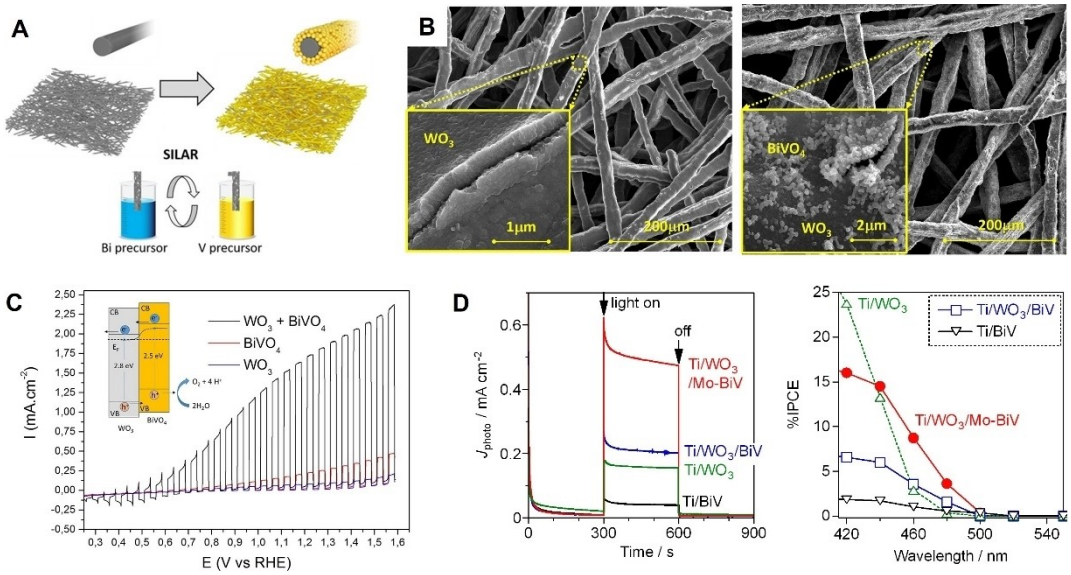

Figure 5. (A) Successive ionic-layer adsorption and reaction (SILAR) cycles for the preparation of $BiVO_4$ layers on porous substrates.[14] (B) SEM images of WO_3 and $WO_3/BiVO_4$ layers coated on Ti felt. (C) Linear sweep voltammograms of porous photoanodes in 0.1 M H_2SO_4 (pH 1.0) under chopped visible light irradiation (> 395 nm, 100 mW cm^{-2}) and the proposed charge-separation mechanism operating in the $WO_3/BiVO_4$ heterojunction. (D) Photocurrent responses under blue light (454 nm LED, 12 mW cm^{-2}) and IPCE action spectra of porous photoanodes on Ti felt in 0.1 M NaPi (pH 6.8) at 1.20 V vs. RHE (BiV; $BiVO_4$, Mo-BiV: Mo-doped $BiVO_4$).[15] Adapted from Ref. [14,15]. Copyright (2017 and 2020), with permission from Elsevier and the American Chemical Society.

deposition of Rh/Cr_2O_3 and CoOOH co-catalysts.[29] Amano *et al.* prepared a $SrTiO_3$ layer on Ti-fiber felt substrates using a hydrothermal reaction of a TNTA layer in 25 mM $Sr(OH)_2$ at 150 °C for 2 h (Figure 6A).[4] The anatase TNTA layer was prepared by electrochemically anodizing Ti felt followed by calcination at 550 °C. The hydrothermally obtained $SrTiO_3$ layer was further calcined in air at 550 °C for 1 h to increase its crystallinity. While the nanotube structures were retained during the hydrothermal reaction, calcination resulted in column-like vertically interconnected $SrTiO_3$-nanoparticle structures (~60 nm).

Figure 6B shows the PEC activities of porous TNTA and $SrTiO_3$ photoanodes in a neutral aqueous electrolyte (pH 6.7) under UV irradiation (365 nm LED, 40 mW cm^{-2}).[4] The cyclic voltammograms reveal that TNTA exhibits higher J_{photo} values than $SrTiO_3$ at high potentials. In contrast, the photocurrent onset potential of the $SrTiO_3$ layer (0.25 V vs. RHE) was more negative than that of the TNTA layer (0.44 V vs. RHE), and corresponded to the negative shift (0.25–0.30 eV) in the flat-band potential of the $SrTiO_3$ layer compared with that of the TNTA layer. The $SrTiO_3$ layer exhibited an inferior photocurrent response than the TNTA layer at high applied potentials (1.6 V vs, RHE); however, they were similar at 0.6 and 0.9 V (vs. RHE). Interestingly, the $SrTiO_3$ layer even exhibited a J_{photo} of 0.60 mA cm^{-2} at 0.3 V (vs. RHE) while TNTA did not exhibit a response at low potentials. This result is consistent with the cathodic shift in the photocurrent onset observed by cyclic voltammetry. The porous $SrTiO_3$ photoanode was also active toward vapor-fed water splitting at an applied bias of only 0.3 V in a PEM-PEC cell (RH $<$100%), aided by PFSA-ionomer functionalization.

2.2.5. Fe_2O_3 on felt

α-Fe_2O_3 (hematite) is an n-type oxide material that is also inexpensive owing to its natural abundance. Importantly, its bandgap (~2.1 eV) facilitates its ability to absorb most of the visible light in the solar spectrum.[30] Fe_2O_3 photoanodes with 3D porous structures were hydrothermally prepared on Ti felt at 393 K, followed by two-step annealing in air at 873 K and in argon at 473 K.[5] Ti-doped Fe_2O_3 on porous Ti felt exhibited a higher J_{photo} value than flat FTO glass or Ti sheets. Ti^{4+} doping increased the donor density of the Fe_2O_3 layer via the second annealing step in the absence of oxygen.[8] Ti-doped Fe_2O_3/Ti-felt was further modified by an Al_2O_3 passivation layer and a cobalt phosphate (CoPi) OER co-catalyst; porous Ti-doped Fe_2O_3-Al_2O_3-CoPi exhibited a J_{photo} of 0.85 mA cm^{-2} at 1.23 V vs. RHE in 1 M NaOH (pH 13.6) under 1-sun illumination (AM1.5G).[31] The relatively lower performance would be improved by adopting reported preparation methods for the highly efficient hematite photoanodes.

2.3. Photocathodes on felt substrates

In p-type semiconductors, the electrons as a minority carrier photoexcited in the bulk need to move to the solid-liquid interface without recombining with holes to induce photocathodic reactions. Long-distance migration in a thick film, which is required to absorb sufficient light, leads to performance saturation or deterioration in a 2D dense photocathode. A 3D porous structure provides significantly larger interfaces; consequently, thin films with shorter diffusion distances that efficiently promote surface reactions can be used.

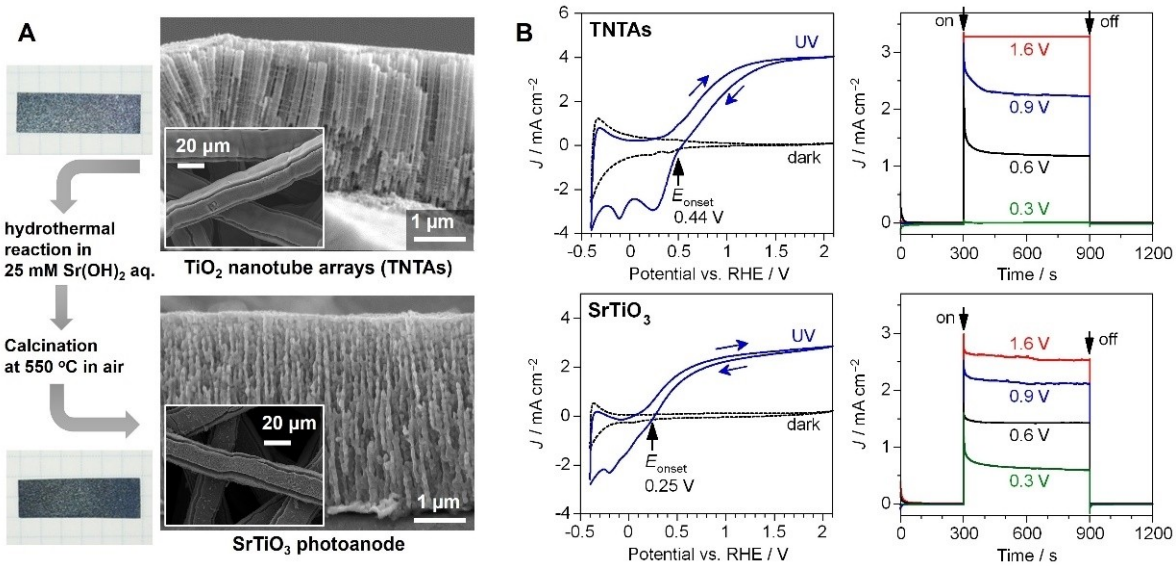

Figure 6. (A) Scheme showing the preparation of a $SrTiO_3$ layer from a TiO_2 nanotube array (TNTA) layer on Ti felt and corresponding SEM images of the top (inset) and cross-sectional views. (B) Cyclic voltammograms and photocurrent responses at various applied potentials (V vs. RHE) for TNTA and $SrTiO_3$ layers on Ti felt in 0.2 M Na_2SO_4 with 0.1 M NaPi buffer (pH 6.7) under UV irradiation (365 nm LED, 40 mW cm^{-2}). The photocurrent onset potential (E_{onset}) was determined from the cross-sections of curves acquired in the dark and when photoirradiated during backward scanning. Adapted from Ref. [4]. Copyright (2020), with permission from the Royal Society of Chemistry.

2.3.1. $CuInS_2$ on felt

Copper-based chalcopyrite semiconductors, such as $CuInS_2$ and Cu(In, Ga)Se_2, have been studied as p-type semiconductors for photovoltaic and PEC applications. In 2017, Abe *et al.* reported the use of arc-plasma deposition and subsequent annealing under a stream of dilute H_2S to prepare p-type $CuInS_2$ on carbon felt.[12] Firstly, CMF was calcined at 500 °C (for 30 min) to generate a hydrophilic surface. Metallic Cu and In cathodes were used as elemental arc-discharge sources under vacuum at room temperature. The Cu/In ratio in the deposited film was found to be homogeneous, even inside the 3D network, whereas the conventional electrodeposition method resulted in segregation. The selection of appropriate conditions (capacitance and voltage) is indispensable for achieving favorable arc-plasma deposition. Sulfurization, led to the formation of an almost full-coverage $CuInS_2$-layer coating on the 3D CMF structure, as shown in Figure 7A. The prepared $CuInS_2$/CMF photocathode was modified using a thin CdS layer and Pt particles. The Pt-CdS/$CuInS_2$/CMF photocathode exhibited higher PEC water-reduction performance than conventional Pt-CdS/$CuInS_2$ fabricated on a 2D Mo substrate, which highlights the superiority of the porous high-surface-area structure. An IPCE value of approximately 40% was determined in 0.5 M aqueous Na_2SO_4 under 600 nm light at 0 V (vs. RHE).

2.3.2. Cu_2O on felt

Cuprous oxide (Cu_2O) is a low-cost p-type semiconductor oxide as a solar-energy-conversion candidate. Cu_2O photocathodes were fabricated on macroporous Ti-felt substrates by a facile electrodeposition method.[6] This study compared the PEC performance of Cu_2O/Ti-felt with that of Cu_2O films on conventional 2D conductive substrates (FTO glass and Ti sheet). Electrodeposition was performed in 0.2 M aqueous copper lactate at pH 11 and 65 °C, and the loading amount was controlled by the electric charge density (0.5 and 3.0 C cm^{-2}) applied during the reduction of Cu^{2+} to Cu_2O. Figure 7B shows images of Cu_2O/Ti-felt prepared at −0.4 V vs. Ag/AgCl (0.5 C cm^{-2}), which reveal that the entire surface of the Ti felt is covered by the Cu_2O layer. The cross-sectional SEM image shows that the Cu_2O layer is deposited as dense polycrystals with an average thickness of about 0.1 μm; however, it was not particularly homogeneous. A higher current density was observed for the potentiostatic electrodeposition on Ti felt than on the Ti plate owing to its porous structure; the Ti felt has a six-fold-larger surface area than the Ti plate at a thickness of 0.2 mm. The amount of loaded Cu_2O film monotonically increased with increasing charge density owing to the almost 100% Faradaic efficiency of the Cu_2O formation process.

The PEC properties of Cu_2O/Ti-felt electrodes were explored by reducing methyl viologen ($E(MV^{2+}/MV^{\bullet+}) = -0.45$ V vs. SHE) in the presence of oxygen at pH 5.3. The porous Cu_2O photocathodes exhibited higher photocurrent response than 2D dense Cu_2O electrodes. The Cu_2O layer (~0.1 μm) on Ti felt exhibited a superior J_{photo} value compared to that of a thick Cu_2O layer (~0.6 μm) on conventional Ti-sheet or FTO-glass. The enhanced PEC properties are attributable to the larger Cu_2O | electrolyte and Cu_2O | substrate interfaces rather than the effect of film thickness because a thick Cu_2O layer (~0.5 μm) on Ti felt also exhibited a high J_{photo} value. The large interfaces provided by the macroporous structure are beneficial for photoexcited electron transfer to MV^{2+} and hole transport to conductive substrates, as shown in Figure 7B.

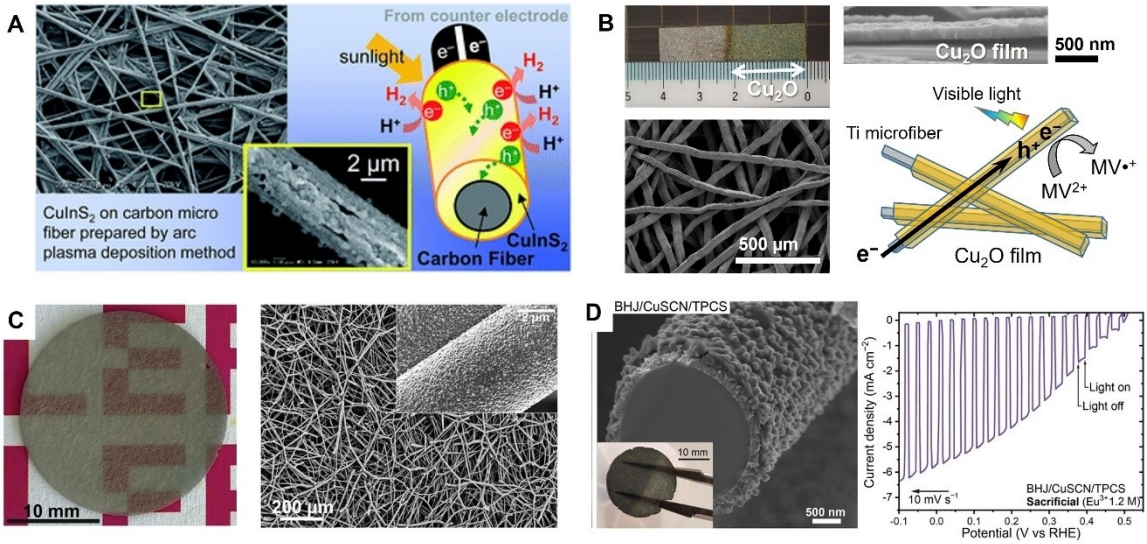

Figure 7. (A) Porous $CuInS_2$ on carbon microfibers for the PEC hydrogen-evolution reaction.[12] (B) Porous Cu_2O photocathodes on Ti fibers for the PEC reduction of methyl viologen (MV^{2+}) to the corresponding cation radical.[6] (C) Photographic and SEM images of FTO-coated transparent porous conductive substrates (TPCS).[13] (D) Photographic and SEM image of a bulk-heterojunction (BHJ)/CuSCN/TPCS photocathode and its PEC response toward Eu^{3+} reduction (pH 2) under 1-sun simulated illumination (AM1.5G, 100 mW cm^{-2}). Adapted from Ref. [6,12,13]. Copyright (2017, 2020, and 2023), with permission from the Royal Society of Chemistry, Elsevier, and Wiley-VCH.

2.3.3. Transparent felt substrates

Recently, Sivula *et al.* reported a transparent porous conductive substrate (TPCS) based on an FTO-coated SiO_2-interconnected fiber-felt substrate.[13] Optically transparent conducting materials are required for optoelectronic applications. However, porous conductive substrates are typically composed of graphitic carbon or metallic materials and are not light transmissive. Moreover, freestanding TPCS has not yet been reported. Figure 7C shows the TPCS obtained by coating fused SiO_2 fiber felt with an FTO layer using atmospheric chemical vapor deposition at 600 °C. The SiO_2-fiber felt itself was prepared by thermal sintering of vacuum-filtered quartz fibers (fiber diameter: 2–5 μm) at 1250 °C for 2 h to connect fiber intersections. A 100 nm conformal coating of the FTO layer afforded a sheet resistivity of ~20 $\Omega\,sq^{-1}$ and a 41% loss of incident light at 550 nm, which demonstrates the semitransparency of the porous substrate.

The TPCS can be coated with various semiconductors, including *n*-Fe_2O_3 (chemical bath deposition), *p*-CuSCN, *p*-Cu_2O (electrodeposition), and conjugated polymers (dip coating).[13] The observed PEC performances were similar to those of the corresponding photoelectrodes on flat substrates, which demonstrates that TPCS is suitable for PEC applications. Figure 7D shows SEM images of the donor-acceptor bulk-heterojunction (BHJ) coating on CuSCN/TPCS. The π-conjugated-polymer BHJ layer is designed to overcome the limitations associated with the short exciton lifetime and improve the photoenergy conversion efficiency in organic solar cells.[13] TPCS had previously been coated with copper(i) thiocyanate (CuSCN) via electrodeposition; CuSCN is composed of nanorods that are approximately 300 nm in height and act as a hole-transporting layer. The BHJ blended PBDTTTPD:P(NDI2HD-T) donor-acceptor combination was deposited on CuSCN/TPCS by the dip-coating method. The BHJ/CuSCN/TPCS photocathode delivered a J_{photo} of -6 mA cm^{-2} in 1.2 M aqueous $Eu(NO_3)_3$ (pH 2) at 0 V (vs. RHE) under 1-sun illumination, and the platinized-BHJ/CuSCN/TPCS photocathode showed a J_{photo} of 1 mA cm^{-2} (at 0 V vs. RHE) in a half-gas-phase PEC cell; however, the HER Faradaic efficiency, defined as the percentage of passed electrons leading to hydrogen formation, was only 40%.

3. Polymer electrolyte photoelectrochemistry

Porous photoelectrodes exhibit superior gas diffusion and mass transport properties. The porosity inside the photoelectrode is necessary when it is used with a solid polymer electrolyte such as PEM and AEM. The membrane photoelectrode assemblies are promising for advanced PEC systems to facilitate mass-transport-limited reactions. The PEM-PEC system has been applied for hydrogen production using pure liquid water or air humidity.

3.1. Pioneering PEM-PEC-cell studies

Nafion® (Chemours) and Aquivion® (Solvay), which are common PEMs, are highly proton-conductive and can shorten the inter-electrode gap because the gaseous product is separated in each compartment. In 1996, Ichikawa reported a PEC system composed of a porous TiO_2 photoanode and an electrocatalyst cathode, in which a Nafion membrane was placed between the electrodes to form a single unit.[34] Porous electrodes that passed protons perpendicular to the surface were used. Hydrogen-evolution and CO_2-reduction reactions were examined under unbiased and biased conditions using the TiO_2/Ti photoanode in 0.1 M aqueous $KHCO_3$ under UV light, which delivered a hydrogen-production rate of 42 μL h^{-1} cm^{-2} under sunlight without applied bias.

In 2009, Kamat *et al.* introduced a PEC reactor for producing solar hydrogen based on the principles of a PEM-based fuel cell.[32] Figure 8A shows a schematic of a PEM-PEC cell with two graphite flow-field plates. In the membrane electrode assembly, TiO_2 P25 particles and platinized carbon black (Pt-CB) deposited on carbon paper were hot-pressed on opposite sides of the PEM (Nafion 117) as the photoanode and cathode, respectively. SEM images show that TiO_2 (3.0 mg cm^{-2}) and Pt-CB (0.5 mg cm^{-2}) particles are uniformly dispersed on each carbon fiber; this porous structure provides a high surface area and facilitates mass transfer. Flowing 0.1 M H_2SO_4 containing different concentrations of methanol was continuously circulated in the photoanode chamber under UV irradiation ($\lambda > 300$ nm, 100 mW cm^{-2}). The short-circuit photocurrent was observed to increase with increasing methanol concentration, with a value of 0.35 mA cm^{-2} recorded for 1 M methanol. Hydrogen was continuously produced at a rate of 69 μL h^{-1} cm^{-2} in N_2-purged 0.1 M H_2SO_4 without bias. The photogenerated holes were then consumed by methanol, which decomposes into CO_2 and protons that can be transported through the PEM to the cathode and reduced by the photoexcited electrons that pass through the external circuit to form hydrogen. The PEC properties of similar TiO_2(P25) | PEM | Pt-CB cells were investigated under UV irradiation in several liquid solutions, including pure water.[35] Operation in the vapor phase resulted in a photocurrent decay, from 40 to 2 μA, over 2 h of illumination due to membrane dehydration.

PEM-PEC cells can be used to split pure water and for gas-phase reactions without liquid electrolytes. In 2009, Georgieva *et al.* provided proof-of-concept for gas-phase photoelectrochemistry by developing an all-solid PEC cell for the photooxidation of methanol vapor (Figure 8B).[33,36,37] The photoanode consisted of electrodeposited WO_3 and TiO_2 on stainless-steel mesh using Na_2WO_4 and $TiOSO_4$ solutions. The SEM image shows the uniformly distributed cracked-mud morphology of the TiO_2/WO_3 bilayer coated on the mesh surface. These "mud cracks" comprise WO_3 flakes decorated with smaller TiO_2 particles. A PEC cell was constructed by attaching the TiO_2/WO_3 mesh photoanode and a Ag/AgCl reference electrode to one side of a Nafion membrane, and a stainless-steel mesh on the other side as the counter electrode. The gas-phase PEC reaction was performed in air containing water and methanol vapors at

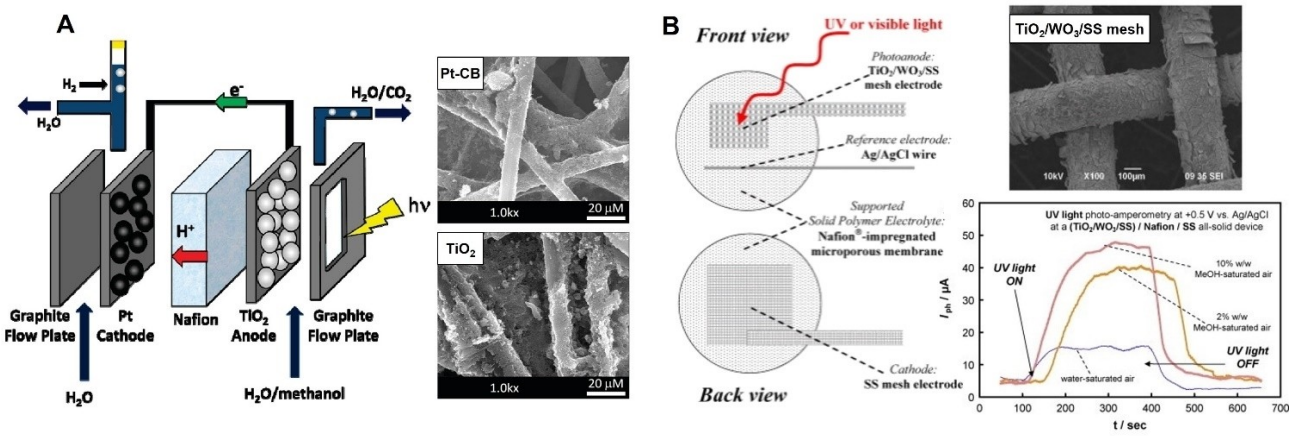

Figure 8. (A) Schematic of a PEM-PEC cell based on a methanol fuel cell consisting of a TiO_2 photoanode and a platinized carbon-black (Pt-CB) cathode deposited on gas-diffusion carbon paper.[32] The membrane electrode assembly was inserted into graphite flow-field plates and aqueous methanol was continuously fed into the photoanode compartment to consume photogenerated holes. (B) Schematic of the all-solid-state PEC cell used to oxidize gas-phase methanol.[33] A TiO_2/WO_3/stainless-steel (SS) mesh photoanode and a Ag/AgCl wire reference electrode were attached to the front side of a Nafion-impregnated membrane, while the SS cathode was attached to the backside. SEM image of the TiO_2/WO_3/SS mesh photoanode and photocurrent responses of the PEM-PEC cell in a stream of air saturated with water and methanol (2% and 10%) vapors under UV irradiation. Adapted from Ref. [32,33]. Copyright (2009), with permission from the American Chemical Society and Elsevier.

0.5 V vs. Ag/AgCl under UV illumination ($\lambda_{max} = 369$ nm, 3 mW cm^{-2}). The J_{photo} was small under water-vapor feed but increased with increasing methanol concentration, which indicates that methanol acts as a scavenger for photogenerated •OH or holes. Various photoanodes based on TiO_2 P25 and mixed carbon powders have also been reported for gas-phase PEC reactions.[38]

3.2. Vapor-fed PEM-PEC water splitting

PEC water splitting is traditionally performed using aqueous electrolytes (typically corrosive acids or alkaline solutions) to produce hydrogen; however, the use of liquid electrolytes in this process has some disadvantages, including the formation of gas bubbles, costs associated with freshwater supply, the energy required to pump liquids, freezing at low temperatures, and low device durability.[41,42] Gas bubbles formed during the OER scatter light and block catalytic active sites, which reduces efficiency. The need for freshwater to avoid catalyst, photoelectrode, and membrane poisoning requires energy-intensive water-purification or seawater-desalination processes. To circumvent these limitations in terms of commercial feasibility, the utilization of water vapor in ambient air as a hydrogen-production source has recently attracted attention. Humidity exists even in water-scarce geographical areas and can be fed by natural convection without purification.[43] Therefore, the use of water vapor may extend the applicability of this technology to rural and off-grid areas with abundant sunlight. The lack of contact with liquid electrolytes is expected to prevent (photo)corrosion by improving durability and reducing the risk of environmental contamination from spillage and the leaching of toxic components from the PEC device.

Martens *et al.* developed a PEM-PEC cell and demonstrated unbiased hydrogen production from the water vapor present in air (Figure 9A).[39] Hierarchically structured electrodes were prepared by coating a carbon-fiber substrate with multi-walled carbon nanotubes (MWCNTs) using the dip-coating method and a TiO_2 thin film using atomic layer deposition (ALD). ALD is a conformal coating method to control the thickness of a uniform thin film by alternating the exposure to a chemical precursor, followed by hydrolysis/oxidation. MWCNTs coated with anatase TiO_2 thin film (~10 nm thick) were prepared and the structure was confirmed even after heating at 550 °C in air (Figure 9B). The cathode was also prepared by depositing Pt nanoparticles (~5 nm) on the MWCNTs using ALD, and a membrane-electrode assembly was prepared by directly fixing gas-diffusion electrodes to each side of a PEM. Nafion ionomer and zeolite (hydrating stub) particles were drop-cast onto the electrodes to enhance proton conductivity toward the membrane; the zeolite ensured Nafion-ionomer proton conductivity in low humidity. The PEC performance of the TiO_2/MWCNT photoanode was evaluated at 25 °C in an unbiased PEM-PEC cell open to the outside air (60% RH) (Figure 9C). The cathode compartment was sealed under dry nitrogen after flushing to analyze hydrogen production. After an initial induction period, a stable photocurrent of 5.5 μA cm^{-2} was obtained under simulated solar light (AM1.5G, 100 mW cm^{-2}) for 24 h. The HER Faradaic efficiency was determined to be close to 100%. A hydrogen-production rate of 85 nmol h^{-1} cm^{-2} (RH 55% at 26 °C) was recorded under natural sunlight, with a maximum value of 148 nmol h^{-1} cm^{-2} observed at noon (Figure 9D).

Norby *et al.* also developed PEM-PECs for the oxidation of gaseous reactants under UV-visible irradiation.[40,44,45] The TiO_2(P25) | PEM | Pt-CB cell exhibited a low J_{photo} value in humidified Ar even with applied voltage; however, this increased to 250 μA cm^{-2} in the presence of methanol vapor.[44] TiO_2 particles were prepared on a carbon-paper substrate using Nafion ionomer as the adhesive. The hydrating effect of the Nafion molecules that surround the TiO_2 particles was consid-

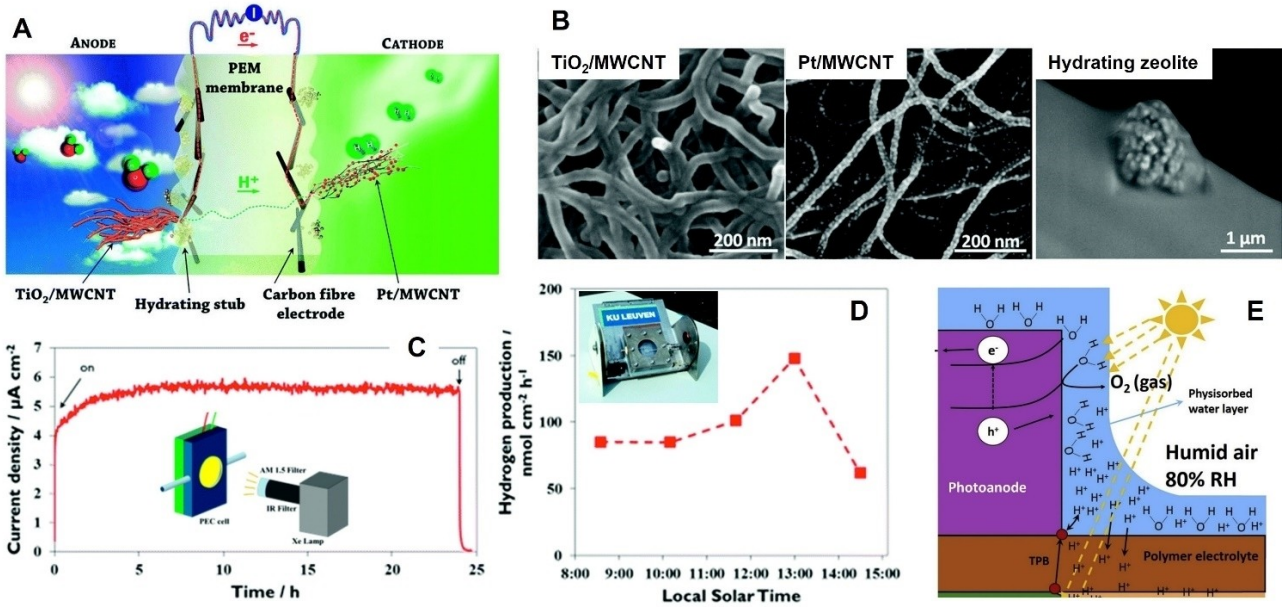

Figure 9. (A) Schematic depicting an air-based PEM-PEC cell for producing hydrogen from ambient humidity (TiO_2/MWCNT: TiO_2 layer coated on a multi-walled carbon nanotube, hydrating stub: zeolite for capturing water molecules in the air, carbon fiber electrode: gas-diffusion porous substrate, and Pt/MWCNT: Pt nanoparticles dispersed on MWCNT).[39] (B) SEM images of the TiO_2/MWCNT photoanode, Pt/MWCNT cathode, and the zeolite embedded in the Nafion ionomer on TiO_2/MWCNT. (C) J_{photo} of the air-based PEM-PEC cell under simulated solar light illumination (AM1.5G, 100 mW cm^{-2}). (D) Hydrogen production rates from PEM-PEC cells in outdoor air and natural sunlight at various times of the day. (E) The proton-transport concept toward the membrane through a water layer physically adsorbed on the photoanode surface in humidified air (80 % RH).[40] Adapted from Ref. [39,40]. Copyright (2014 and 2019), with permission from the Royal Society of Chemistry and Elsevier.

ered to deliver methanol to the photoanode for more-efficient electron transfer to photogenerated holes.

In addition to their early work, Norby *et al.* introduced the concept of surface proton conduction in water layers adsorbed on TNTAs grown on Ti-mesh substrates.[40,45] The CdS/TNTAs | PEM | Pt-CB cell delivered a J_{photo} of 0.44 mA cm^{-2} at 1.23 V (vs. the cathode) under one-sun simulated illumination in humidified air (80 % RH).[45] They proposed a proton-conduction mechanism involving continuous liquid-like water layers adsorbed on the oxide surface rather than one in which the ionomer contacts the photoanode, even though the Nafion ionomer was used as a binding agent in the membrane electrode assembly (Figure 9E).[40]

The importance of the surface water layer in a photocatalytic system has also been highlighted in a recent review article.[46] GaN:ZnO (bandgap: 2.68 eV) is active toward water splitting when loaded with a Rh-Cr mixed-oxide ($Rh_{2-y}Cr_yO_3$) co-catalyst. The apparent quantum efficiency, which is defined as the number of electrons that contribute to the reaction divided by the number of incident photons, was determined to be 5.5 % for $Rh_{2-y}Cr_yO_3$/GaN:ZnO powder suspended in liquid-phase pure water under 350 ± 10 nm light. In contrast, the apparent quantum efficiency in flowing 65 %-RH helium at 25 °C was only 0.16 % under 367 nm light (UV LED).[47] The photocatalytic activity when vapor-fed is strongly dependent on the RH because adsorbed water layers have limited proton conductivities. It should be noted here that post-gas separation is required to obtain pure hydrogen in the photocatalytic system, and that efficiency is diminished in the presence of oxygen (21 % in air) owing to the reverse water-forming reaction, different from the PEC system.

3.3. PFSA-functionalized porous photoanodes

Electrocatalyst layers functionalized with ionomers (typically the PFSA ionomer) have been used in polymer electrolyte fuel cells and electrolysis cells. Here, fixing catalyst particles onto gas-diffusion/porous-transport layers is one of the functions of these layers, while another function involves forming triple-phase (gas-electrolyte-catalyst) boundaries that promote efficient proton-coupled electron-transfer reactions. Inspired by the triple-phase boundary concept, a strategy for fabricating PEC triple-phase boundaries (gas-electrolyte-semiconductor interfaces) was proposed by Amano *et al.*[10] Functionalizing porous semiconductor electrodes with the PFSA ionomer is necessary for promoting PEC reactions under gas-fed conditions in the absence of liquid water. The ionomer coating improves proton conductivity on the photoanode surface owing to the adsorption of water vapor when gas-fed.

The PEC performance of a porous WO_3 photoanode when fed water vapor (RH < 100 %) was investigated under two cathode conditions (liquid phase and gas phase), as shown in Figure 10A,[10] in which the WO_3 photoanode and the Pt-CB cathode are in contact with the Nafion membrane. The porous WO_3 photoanode exhibited a photocurrent response (IPCE = 9.7 %) for a "gas | solid | liquid" interface (half-gas phase PEC cell) in which the Pt-CB cathode is immersed in an aqueous

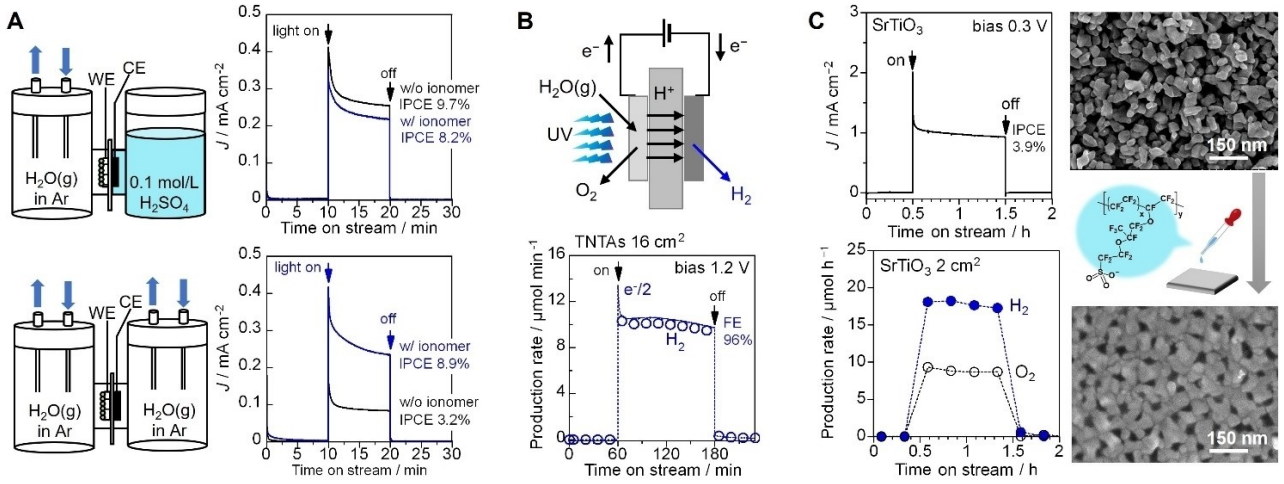

Figure 10. (A) H-type dual-compartment glass reactors for "gas | solid | liquid" and "gas | solid | gas" interfaces. The effect of the PFSA ionomer coating on the photocurrent response of the porous WO_3 photoanode at 1.2 V (vs. the Pt-CB cathode) under blue light (453 nm LED, 6.8 mW cm^{-2}).[10] (B) PEM-PEC cell with an ionomer-functionalized TNTAs/Ti-felt photoanode (irradiation area: 16 cm^2) and a Pt-CB cathode for vapor-fed water splitting (90% RH) and the hydrogen-production time course in the cathode compartment.[7] The reaction was performed under UV light (365 nm, 40 mW cm^{-2}) at 1.2 V (vs. the cathode). (C) Vapor-fed water splitting (90% RH) by a PEM-PEC cell with an ionomer-functionalized $SrTiO_3$/Ti-felt photoanode (irradiation area: 2 cm^2) and a Pt-CB cathode under UV light (365 nm, 42 mW cm^{-2}) at 0.3 V (vs. cathode).[4] Surface SEM images of the $SrTiO_3$ photoanode with and without a Nafion ionomer coating (2.4 mg cm^{-2}). Adapted from Ref. [4,7,10]. Copyright (2018, 2019, and 2020), with permission from Amano *et al.*, Wiley-VCH, and the Royal Society of Chemistry.

electrolyte (0.1 M H_2SO_4), even without ionomer functionalization. In contrast, the bare photoanode exhibited an IPCE value less than that of the ionomer-coated photoanode for a "gas | solid | gas" interface in which no liquid water was present in the reactor. These results highlight the importance of surface-ionomer functionalization in fully gas-based PEM-PEC cells. The ionomer coating not only enhances the IPCE of the WO_3 photoanode but also improves the Faradaic efficiency for the evolution of O_2 in the vapor-fed water-splitting reaction, which suggests that the PEC triple-phase boundary enhances proton-coupled electron transfer in the OER.

The surface-ionomer-coating strategy was applied to a Mo-doped $BiVO_4/WO_3$/Ti-felt photoanode used to split water vapor under visible light.[15] The PEM-PEC cell exhibited an IPCE of 10% when fed water vapor (90% RH) at 1.2 V (vs. the cathode) under 454-nm light, with H_2 and O_2 Faradaic efficiencies of 100 and 94%, respectively. Tsampas *et al.* also reported a surface-functionalized photoanode system for PEC hydrogen production using humidified air (100% RH) as the only water source, resulting in 1.55 mA cm^{-2} at 1.23 V (vs. RHE) under AM1.5G simulated solar light.[11] Porous W-doped $BiVO_4$ functionalized by an Aquivion ionomer coating delivered 70% of the J_{photo} value recorded in a liquid electrolyte (0.1 M Na_2SO_4, pH 6.0) probably because the ionomer adsorbs water molecules from humid air.

A PFSA-ionomer-coated TNTA photoanode exhibited a high IPCE (16%) even in a large PEM-PEC cell (16 cm^2) when fed water vapor (90% RH).[7] A J_{photo} value of 2 mA cm^{-2} was recorded under UV light (365 nm, 40 mW cm^{-2}), with a HER Faradaic efficiency of 100%, and a hydrogen-production rate of 600 μmol h^{-1}, which corresponds to 14.7 mL h^{-1} (Figure 10B). In addition, the PEC properties of the ionomer-coated TNTA photoanode were unaffected by the presence of the 21 vol% O_2 in the air compared to the use of humidified argon. Therefore, the PEM-PEC system can be adapted to be an air-based H_2-production system using the humidity in ambient air.

As previously reported for a TiO_2(P25) | PEM | Pt-CB cell, the TNTA photoanode generated photocurrent with hydrogen evolution without a bias voltage.[7] However, this hydrogen evolution is not due to overall water splitting because CO_2 was the major product on the TiO_2 photoanode (due to the decomposition of the PFSA membrane and ionomer) rather than O_2 at low applied voltages. In contrast, the ionomer-coated $SrTiO_3$ photoanode promoted the OER with a Faradaic efficiency greater than 99%, even at low potentials.[4] The vapor-fed $SrTiO_3$ | PEM | Pt-CB cell induced overall water splitting, as evidenced by the 2:1 ratio of H_2:O_2 evolved at 0.3 V (vs. the cathode) (Figure 10C). A J_{photo} value of 0.93 mA cm^{-2} (IPCE 3.9% at 365 nm, 40 mW cm^{-2}) and a H_2-evolution rate of 17.3 μmol h^{-1} (irradiation area 2 cm^2) were recorded upon the surfaces of the $SrTiO_3$ particles enwrapped by PFSA ionomer thin films. The proton conductivity of the hydrated ionomer enhanced charge transfer from the adsorbed water to the photogenerated holes on the photoanode surface.

The bare photoanode (porous rutile TiO_2) exhibited a low photocurrent response at RH values less than 100% (Figure 11A).[21] In contrast, J_{photo} was enhanced by the Nafion ionomer coating owing to the formation of a PEC triple-phase boundary that captured water vapor in the gas phase. The J_{photo} value at 1.2 V (vs. the cathode) gradually increased as the number of ionomer coatings was increased, while the amount of loaded ionomer increased linearly with the number of coatings (about 0.5 mg cm^{-2} per coating). A maximum J_{photo} was recorded at an ionomer loading above 2 mg cm^{-2}, with an IPCE value (17%) consistent with the performance observed in an aqueous electrolyte (pH 6.7). Enhanced proton-coupled electron

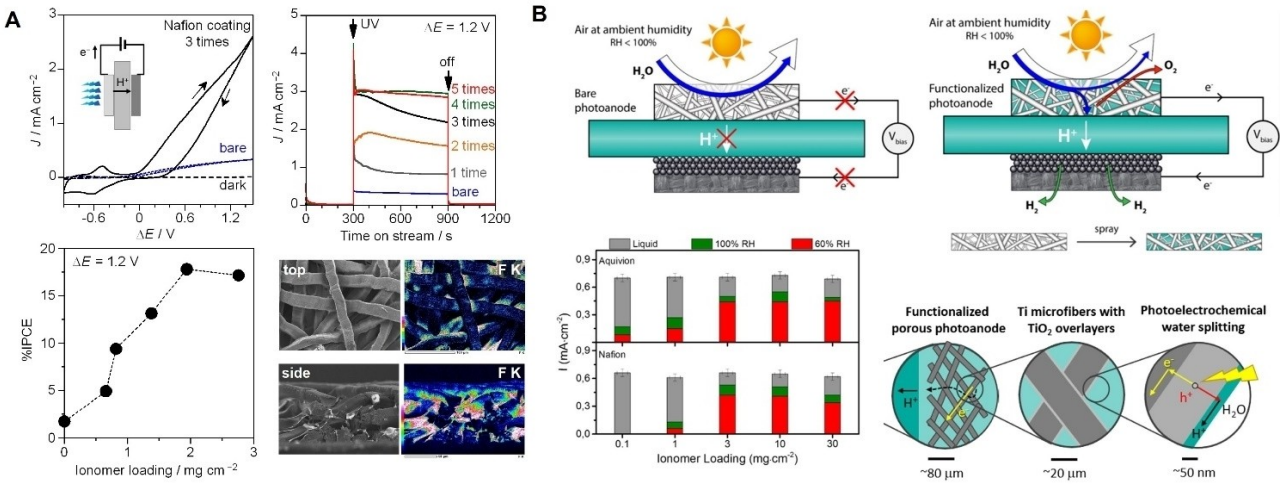

Figure 11. (A) PEC properties of a PEM-PEC cell comprising a rutile-TiO_2/Ti-felt photoanode and a Pt-CB cathode under vapor-fed conditions (RH 90%) irradiated with UV light (365 nm, 40 mW cm^{-2}).[21] (top) Cyclic voltammograms and photocurrent responses at 1.2 V (vs. the cathode) of rutile-TiO_2/Ti-felt photoanodes coated for different times with the Nafion ionomer. (bottom left) IPCE at 1.2 V as a function of Nafion-ionomer loading. (bottom right) SEM-EDS images of the porous photoanode after Nafion-ionomer coating (2.4 mg cm^{-2}). (B) Schematic depicting membrane electrode assemblies with a bare porous photoanode and a functionalized porous photoanode.[27] The porous photoanode was functionalized by spray-coating with a PFSA ionomer. (bottom left) PEC responses of functionalized porous TiO_2 photoanodes coated with the Aquivion (top) and Nafion (bottom) ionomers in a liquid electrolyte (0.1 M aq. H_2SO_4) and humidified air at 60% and 100% RH at different ionomer loadings. (bottom right) Enlarged views of the interfaces associated with proton- and electron-transport pathways during PEC water splitting. Adapted from Ref. [21,27]. Copyright (2019), with permission from the Royal Society of Chemistry and the American Chemical Society.

transfer is rationalized by the improved proton conductivity arising from the hydrated ionomer layer on the photoanode surface. The PFSA ionomer also functions as an adsorbent for low concentrations of water vapor, as evidenced by diffuse reflectance IR spectroscopy.[4] SEM in conjunction with energy-dispersive X-ray spectroscopy (EDS) revealed that some ionomers are segregated in void spaces and the middle region of the porous photoanode. However, top and cross-sectional side views confirmed the formation of proton-transport pathways throughout the electrode.

Tsampas *et al.* also investigated the effect of the PFSA ionomer on the performance of a vapor-fed PEM-PEC cell.[11,27] They used a PEM-PEC cell with a reference electrode compartment to compare the performance of a vapor-fed reaction with that of a liquid-phase reaction in a conventional PEC cell. As reported by our group,[4,7,15,21] but distinct from their previous studies,[14,17,18] porous photoanodes devoid of ionomer functionalization did not exhibit photocurrent responses at RH levels below 100%.[11,27] The discrepancy between the two studies is ascribable to the condensation of water vapor in the PEM-PEC cell at RH > 100%. Bare photoanodes were functionalized by impregnating them with Aquivion and Nafion ionomers via spray coating to improve water vapor absorption and proton conductivity under gas-phase conditions without liquid condensation (RH < 100%) (Figure 11B). Ionomer functionalization (> 3 mg cm^{-2}) enhanced the photocurrent at < 100% RH. A J_{photo} value of 0.5 mA cm^{-2} was recorded at 60% RH and 1.23 V vs. RHE. The use of the Aquivion ionomer led to a slightly higher photocurrent owing to its higher water absorbability, especially at low RH values. A vapor-fed activity at 100% RH was 77% of that observed for a conventional liquid electrolyte (0.1 M H_2SO_4, pH 1.0) at 1.23 V vs. RHE.

The ionomer coating on a porous photoanode enhances water-vapor adsorption. The water absorbed by the ionomer reacts with photogenerated holes to produce O_2 and protons when in proximity to the semiconductor surface. Protons are transported through the surface ionomer layer toward the membrane, whereas electrons are conducted toward the cathode through the titanium microfibers (Figure 11B).

3.4. Gas-fed PEM-PEC reactions

In addition to vapor-fed water splitting, PEM-PEC cells with porous photoelectrodes have been used for gas-fed PEC reactions, including the degradation of volatile organic compounds (VOCs) and methane conversion. The oxidation of VOCs, as air pollutants, occurs at the gas-diffusion photoanode, whereas hydrogen is produced at the electrocatalyst cathode.

Verbruggen *et al.* investigated hydrogen production and the abatement of VOCs in air using a PEM-PEC system in the absence of an applied external bias voltage (Figure 12A top).[48] The PEM (Nafion 117) was sandwiched between a TiO_2 P25 photoanode and a Pt-CB cathode supported on Toray paper. The photoanode was irradiated through a transparent quartz plate with a serpentine flow channel by a UVA light source (4 mW cm^{-2}; similar to solar radiation). The VOCs present in air were modeled using gas-phase methanol as an example. Nitrogen gas or air was continuously bubbled into a closed bottle containing 5 wt% aqueous methanol to create methanol vapor at 65% RH. As shown in Figure 12A (bottom), a J_{photo} value 4.5 times higher than that obtained using pure water vapor as the feed gas was obtained using methanol vapor. The J_{photo} value under gas-fed conditions is nearly 30% higher than

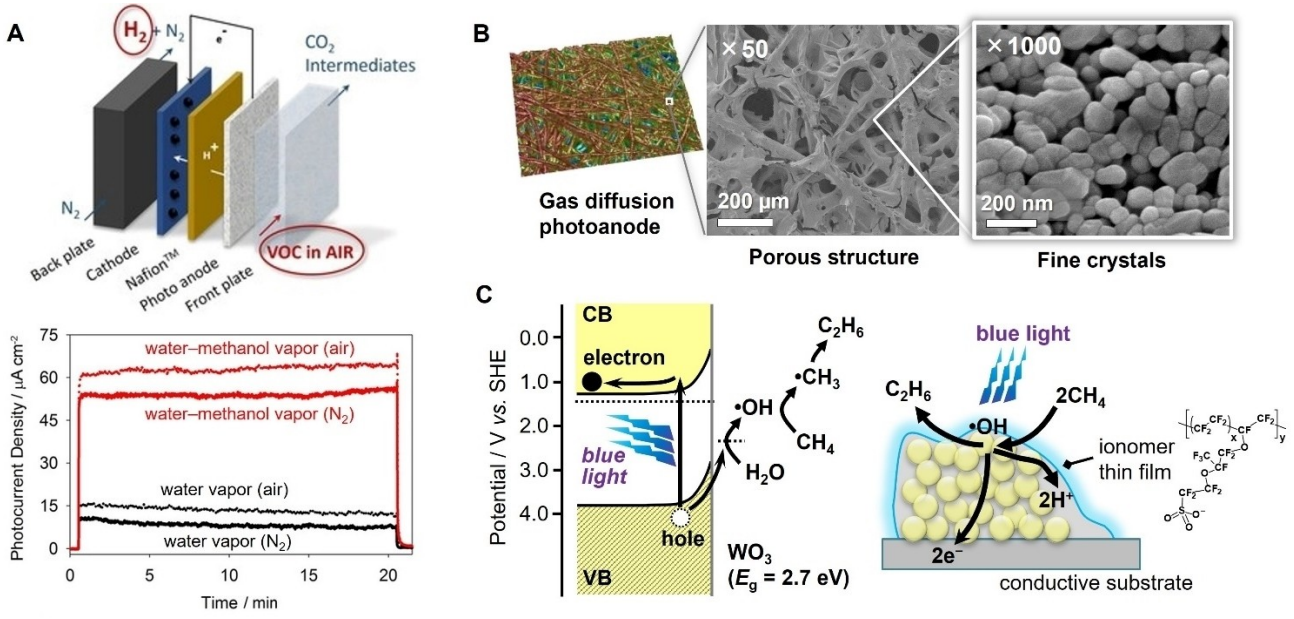

Figure 12. (A) Schematic representation of a PEM-PEC cell used to evolve hydrogen and degrade volatile organic compounds (top).[48] Photocurrent responses of the TiO_2(P25) photoanode when fed pure water vapor in N_2 and air (black traces) and a mixture of methanol and water vapors in N_2 and air (red traces). (B) SEM images of a gas-diffusion WO_3 electrode fabricated on Ti felt.[49] (C) Proposed mechanism for the conversion of methane into ethane on the WO_3 surface and a schematic illustration of the methane-activating triple-phase boundary. Adapted from Ref. [48,49]. Copyright (2017 and 2019), with permission from Wiley-VCH and the American Chemical Society.

that obtained using flowing liquid, which is possibly ascribable to the absence of diffusion limitations in the gas-diffusion photoanode. The photocurrent was slightly lower when air was used as the carrier gas compared to that recorded in inert N_2; the detrimental effect of O_2 was only 8% in the methanol-rich vapor feed, although aerobic oxygen can scavenge photogenerated electrons under unbiased conditions. The authors emphasized that the present system has dual applications: the treatment of VOCs in air and the production of energy in the form of hydrogen. After 30 min of UV irradiation, 0.044 mL of hydrogen was produced in the cathode compartment, with an FE of 92%. Thus, PEM-PEC cells with porous photoanodes can be used to simultaneously degrade air pollutants and produce energy. The J_{photo} value decreased in the order: methanol > ethanol > acetic acid > pure water.

Gas-phase methane conversion was demonstrated using a PEM-PEC cell with a gas-diffusion WO_3 photoanode under visible light (Figure 12B).[16,49] The gas-diffusion photoanode was composed of Ti felt covered with highly crystalline fine WO_3 particles (~100 nm) that interconnected to form a mesoporous structure. A PFSA ionomer was coated onto the surface of the structure to improve the proton conductivity of the bare WO_3 photoanode, thereby creating a triple-phase boundary between the semiconductor particles, ionomer, and methane gas (Figure 12C). Such a triple-phase boundary is beneficial for proton-coupled electron-transfer reactions. Mixtures with different concentrations of methane were flowed into the photoanode compartment with Ar as the balance gas (90% RH at 25 °C) for the gas-fed PEC reaction. The photoanode was irradiated with blue light (453 nm LED, 6.8 mW cm^{-2}) at 1.2 V (vs. the cathode). A photocurrent of approximately 4 mA (irradiation area 16 cm^2) and an IPCE of 11% were recorded in the PEM-PEC cell. O_2 and CO_2, formed by the oxidation of water ($2H_2O_{(g)} \rightarrow O_2 + 4H^+ + 4e^-$) and steam reforming of methane ($CH_4 + 2H_2O_{(g)} \rightarrow CO_2 + 8H^+ + 8e^-$), were the major products under feeding gases with low methane concentrations. In contrast, the ethane production rate increased with increasing methane concentration; a 53.5% selectivity for ethane on a carbon basis was obtained in humidified methane (97% CH_4 and 3% H_2O vapor). Ethane formation is proposed to occur in the following way: Upon irradiation, photogenerated holes oxidize water vapor to form hydroxyl radicals (•OH) that then react with molecular methane to generate methyl radicals ($•CH_3$) that subsequently homocouple to form ethane. Hydrogen was generated at the cathode with a Faradaic efficiency of nearly 100%. These results demonstrate that methane is converted into ethane and CO_2 while hydrogen is concomitantly produced in the PEM-PEC cell under visible light.

3.5. PEC cells with anion-exchange membranes

The use of an α-Fe_2O_3 photoanode with a PEM is limited due to its low acidic tolerance. Hence, another type of polymer electrolyte membrane that is suitable for use in alkaline environments is required. Recently, AEMs with hydroxide ion (OH^-) conductivities have been used with porous Fe_2O_3-based photoanodes.[31] A Ti-doped Fe_2O_3 layer was prepared on a titanium felt substrate and subsequently modified with an Al_2O_3 passivation layer and a CoPi co-catalyst. SEM revealed that the fibrous substrate covered by the Ti-doped Fe_2O_3/Al_2O_3/Co-Pi layer is composed of particles less than 100 nm in size

(Figure 13A). PEC water splitting was achieved in pure water without a supporting liquid electrolyte in a two-compartment cell using the porous Fe_2O_3 photoanode, as shown in Figure 13B. A membrane electrode assembly was prepared by attaching a porous Fe_2O_3-based photoanode to an AEM (Fumapem FAA-3-50). The photoanode and cathode compartments of the AEM-PEC water-splitting system contained pure water and a 1 M NaOH solution, respectively (Figure 13C). Cyclic voltammetry of the AEM-PEC cell showed that Al_2O_3 and CoPi modification led to an improved J_{photo} value (from 0.22 to 0.52 mA cm^{-2} at 1.23 V vs. RHE) (Figure 13D), which is attributable to the passivation layer and co-catalyst that alleviate surface recombination and boost the water-oxidation rate.[3,50,51] The IPCE action spectrum of the Fe_2O_3-based photoanode exhibited an onset wavelength of 600 nm, which corresponds to the bandgap of Fe_2O_3 (~2.1 eV) and is the most extensive wavelength absorption reported for use in polymer photoelectrochemistry (Figure 13E). The porous photoanode and solid electrolyte membrane simultaneously contribute to limiting ion transport in pure water in the absence of a supporting electrolyte. The IPCE of the AEM-PEC cell at 1.2 V (vs. RHE) was 12.7% at 340 nm. However, there is room for further enhancement in the PEC performance of porous Fe_2O_3 by adopting proper preparation techniques.

4. Summary and Outlook

We reviewed macroporous photoelectrodes fabricated using 3D porous substrates, such as carbon paper and Ti felt. The method used to prepare a porous photoelectrode is critical for obtaining high PEC performance for TiO_2, WO_3, $SrTiO_3$, $BiVO_4$, $CuInS_2$, Cu_2O, and organic semiconductors. Generally, porous substrates with high surface areas require uniform and complete coverage of the semiconductor layer with high crystallinity. The open pores and electrical conductivity of the substrate enable the conformal coating via electrochemical deposition and anodization. Thin films on the porous substrates have also been fabricated using solution-based techniques, such as spray coating, dip coating, drop casting, hydrothermal processes, chemical bath deposition, and SILAR. Dry processes, such as ALD, chemical vapor deposition, DC magnetron sputtering, and arc plasma deposition, have also been used to prepare and modify porous electrodes. Porous photoanodes prepared under optimized conditions usually exhibit superior PEC properties compared to conventional 2D flat substrates, such as FTO glass and Ti sheets. A larger specific surface area of the substrate has been shown to provide a larger semiconductor/substrate interface and a shorter distance for photogenerated-charge diffusion, which greatly boosts PEC performance in liquid aqueous electrolytes. The porous photoelectrodes are promising to achieve highly efficient PEC performance by leveraging the preparation strategies and techniques of the stat-of-the-art photoelectrodes. Much research effort is required to increase the crystallinity of the semiconductor nanostructures on porous substrates.

The most attractive feature of porous photoelectrodes is their ability to be used in polymer-electrolyte PEC cells. Gas-diffusion/porous-transport photoelectrodes directly attached to the polymer electrolyte membrane (PEM or AEM) should be

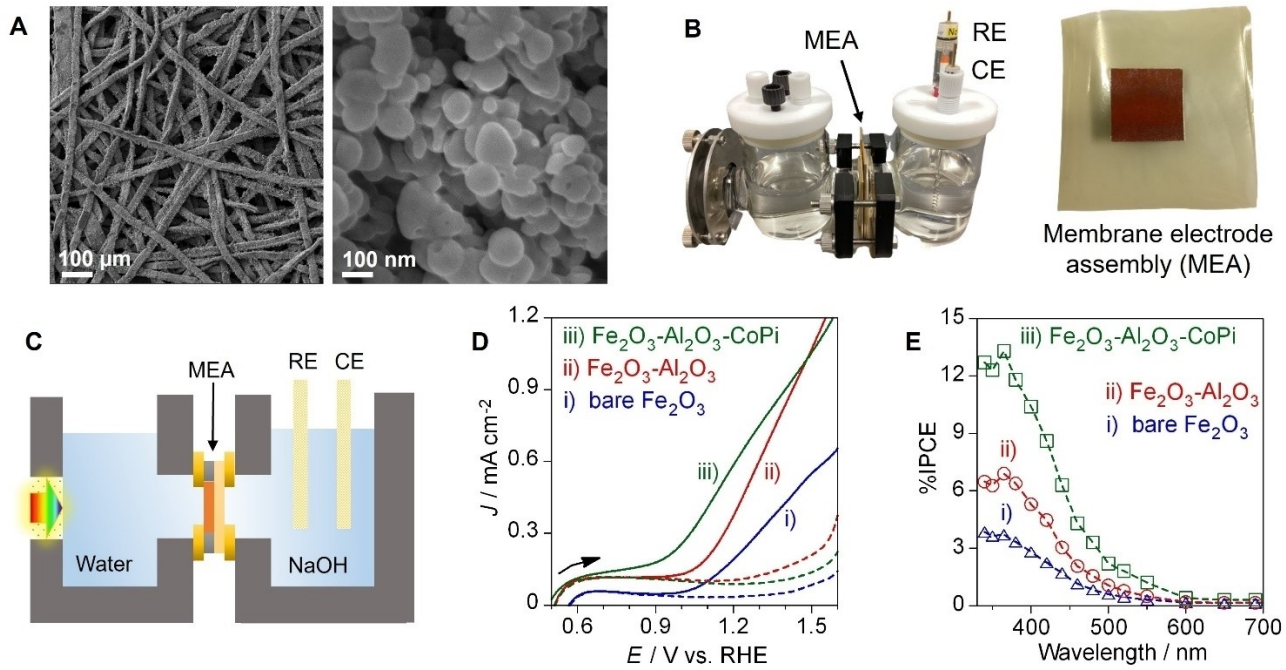

Figure 13. (A) SEM images of a Ti-doped Fe_2O_3-Al_2O_3-CoPi layer fabricated on a porous Ti-felt substrate. (B) PEC-water-splitting set-up and a membrane electrode assembly (MEA) with a porous Fe_2O_3 photoanode and AEM. (C) Schematic of the AEM-PEC cell, in which the photoanode side is filled with pure water while the cathode side contains 1 M NaOH solution with Hg/HgO and Pt counter electrodes. (D) Current densities under simulated solar light irradiation (AM1.5G, 100 mW cm^{-2}) and (E) IPCE action spectra of Ti-doped Fe_2O_3 photoanodes at 1.2 V (vs. RHE) in the AEM-PEC cell. Adapted from Ref. [31]. Copyright (2023), with permission from the American Chemical Society.

highly porous to facilitate proton/anion transport toward the membrane. An additional ionomer thin-film coating on porous photoelectrodes is also important for creating better interfaces between the semiconductors, ionomers, and reactants/products, which are recognized as triple-phase boundaries. A high specific surface area of the semiconductor nanostructures increases the PEC triple-phase contact area, while the porous structure is beneficial for the diffusion and adsorption/desorption of molecules and ions. Membrane-based PEC systems have been used to split pure liquid water and air-based water vapor, oxidatively degrade volatile organic compounds, and induce methane conversion reactions. AEMs have also been used with porous Fe_2O_3 photoanodes for use in pure water in the absence of any supporting liquid electrolyte; however, AEM-PEC systems require further exploration and development.

While the use of porous photoelectrodes and polymer electrolyte-based PEC cells is an encouraging approach for the development of advanced sustainable energy and environmental remediation systems, their performance (efficiency, selectivity, and durability) needs to be further improved based on an understanding of how charge carriers are involved in membrane-based photoelectrochemistry. However, the reaction mechanisms and mass-transport limitations of all-solid-state PEC cells have not been extensively studied. For example, relative humidity greatly affects the hydrogen production rate in a vapor-fed PEC water-splitting system. Better interfacial structures obtained by selecting suitable materials (membrane, ionomer, conductive substrate, semiconductor, passivation layer, and co-catalyst) and controlling multiscale structures (cells, photoelectrodes, and triple-phase boundary) are expected to improve performance.

The goal of the PEC water splitting is to produce hydrogen efficiently using sunlight without external bias. This can be achieved by integrating photoanodes and photocathodes that absorb different parts of the solar spectrum. However, employing a tandem membrane-based PEC system appears challenging because the use of felt substrates reduces light transmittance to the photoelectrode in tandem and the membrane may also affect the transparency. To harvest visible light efficiently, it's essential to develop porous photoelectrodes with narrow bandgaps for solar-to-hydrogen conversion.

In conclusion, porous photoelectrodes effectively enhance the performance of conventional PEC cells in liquid electrolytes and enable advanced membrane systems. Integrated porous photoelectrodes with polymer electrolytes are a promising cutting-edge PEC technology for sustainable energy utilization and environmental remediation. To implement scalable and low-cost PEC devices, porous-transport/gas-diffusion photoelectrodes with high solar energy conversion efficiencies, production rates, selectivities, and stabilities need to be developed by adopting appropriate preparation methods and rationally designed structures.

Acknowledgements

This study was supported by the Japan Society for the Promotion of Science (JSPS) KAKENHI (grant number: JP20H02525).

Conflict of Interests

The authors declare no conflict of interest.

Data Availability Statement

Data sharing is not applicable to this article as no new data were created or analyzed in this study.

Keywords: Photoanode · Photocathode · Porous electrode · Solid polymer electrolyte · Water splitting

[1] A. Fujishima, K. Honda, *Nature* **1972**, *238*, 37–38.
[2] F. Amano, in *Solar-to-Chemical Convers. Photocatalytic Photoelectrochemcial Process.* (Ed.: H. Sun), WILEY-VCH, **2021**, pp. 163–187.
[3] R. Liu, Z. Zheng, J. Spurgeon, X. Yang, *Energy Environ. Sci.* **2014**, *7*, 2504–2517.
[4] F. Amano, H. Mukohara, H. Sato, C. Tateishi, H. Sato, T. Sugimoto, *Sustain. Energy Fuels* **2020**, *4*, 1443–1453.
[5] D. O. B. Apriandanu, S. Nakayama, K. Shibata, F. Amano, *Electrochim. Acta* **2023**, *456*, 142434.
[6] F. Amano, A. Uchiyama, Y. Furusho, A. Shintani, *J. Photochem. Photobiol. A* **2020**, *389*, 112254.
[7] F. Amano, H. Mukohara, A. A. Shintani, K. Tsurui, *ChemSusChem* **2019**, *12*, 1925–1930.
[8] D. O. B. Apriandanu, S. Nomura, S. Nakayama, C. Tateishi, F. Amano, *Catal. Today* **2023**, *411–412*, 113826.
[9] F. Amano, S. Nomura, C. Tateishi, S. Nakayama, *J. Electrochem. Soc.* **2023**, *170*, 026501.
[10] F. Amano, A. Shintani, H. Mukohara, Y. M. Hwang, K. Tsurui, *Front. Chem.* **2018**, *6*, 598.
[11] G. Zafeiropoulos, P. Varadhan, H. Johnson, L. Kamphuis, A. Pandiyan, S. Kinge, M. C. M. van de Sanden, M. N. Tsampas, *ACS Appl. Energ. Mater.* **2021**, *4*, 9600–9610.
[12] H. Homura, O. Tomita, M. Higashi, R. Abe, *Sustain. Energy Fuels* **2017**, *1*, 699–709.
[13] M. Caretti, E. Mensi, R. A. Kessler, L. Lazouni, B. Goldman, L. Carbone, S. Nussbaum, R. A. Wells, H. Johnson, E. Rideau, J. ho Yum, K. Sivula, *Adv. Mater.* **2023**, *35*, 2208740.
[14] T. Stoll, G. Zafeiropoulos, I. Dogan, H. Genuit, R. Lavrijsen, B. Koopmans, M. N. Tsampas, *Electrochem. Commun.* **2017**, *82*, 47–51.
[15] C. X. M. Ta, C. Akamoto, Y. Furusho, F. Amano, *ACS Sustainable Chem. Eng.* **2020**, *8*, 9456–9463.
[16] F. Amano, A. Shintani, T. Sakakura, Y. Takatsuji, T. Haruyama, *Catal. Sci. Technol.* **2023**, *13*, 4640–4645.
[17] T. Stoll, G. Zafeiropoulos, M. N. Tsampas, *Int. J. Hydrogen Energy* **2016**, *41*, 17807–17817.
[18] G. Zafeiropoulos, T. Stoll, I. Dogan, M. Mamlouk, M. de Sanden, M. N. Tsampas, M. C. M. van de Sanden, M. N. Tsampas, *Sol. Energy Mater. Sol. Cells* **2018**, *180*, 184–195.
[19] M. V. Makarova, F. Amano, S. Nomura, C. Tateishi, T. Fukuma, Y. Takahashi, Y. E. Korchev, *ACS Catal.* **2022**, *12*, 1201–1208.
[20] F. Amano, H. Mukohara, A. Shintani, *J. Electrochem. Soc.* **2018**, *165*, H3164–H3169.
[21] F. Amano, H. Mukohara, H. Sato, T. Ohno, *Sustain. Energy Fuels* **2019**, *3*, 2048–2055.
[22] H. Homura, B. Ohtani, R. Abe, *Chem. Lett.* **2014**, *43*, 1195–1197.
[23] H. Homura, O. Tomita, M. Higashi, R. Abe, *J. Photochem. Photobiol. A* **2019**, *375*, 54–63.

[24] F. Amano, A. Shintani, K. Tsurui, Y.-M. Hwang, *Mater. Lett.* **2017**, *199*, 68–71.
[25] F. Amano, S. Koga, *J. Electroanal. Chem.* **2022**, *921*, 116685.
[26] P. Chatchai, Y. Murakami, S. Kishioka, A. Y. Nosaka, Y. Nosaka, *Electrochim. Acta* **2009**, *54*, 1147–1152.
[27] G. Zafeiropoulos, H. Johnson, S. Kinge, M. C. M. M. van de Sanden, M. N. Tsampas, *ACS Appl. Mater. Interfaces* **2019**, *11*, 41267–41280.
[28] C. X. M. Ta, Y. Furusho, F. Amano, *Appl. Surf. Sci.* **2021**, *548*, 149251.
[29] T. Takata, J. Jiang, Y. Sakata, M. Nakabayashi, N. Shibata, V. Nandal, K. Seki, T. Hisatomi, K. Domen, *Nature* **2020**, *581*, 411–414.
[30] K. Sivula, F. Le Formal, M. Grätzel, *ChemSusChem* **2011**, *4*, 432–449.
[31] D. Oky Bagus Apriandanu, R. Marcony Surya, K. Beppu, F. Amano, *ACS Appl. Energ. Mater.* **2023**, *6*, 10736–10741.
[32] B. Seger, P. V. Kamat, *J. Phys. Chem. C* **2009**, *113*, 18946–18952.
[33] J. Georgieva, S. Armyanov, I. Poulios, S. Sotiropoulos, *Electrochem. Commun.* **2009**, *11*, 1643–1646.
[34] S. Ichikawa, R. Doi, *Catal. Today* **1996**, *27*, 271–277.
[35] J. Rongé, D. Nijs, S. Kerkhofs, K. Masschaele, J. A. Martens, *Phys. Chem. Chem. Phys.* **2013**, *15*, 9315–9325.
[36] J. Georgieva, *J. Solid State Electrochem.* **2012**, *16*, 1111–1119.
[37] J. Georgieva, E. Valova, S. Armyanov, N. Philippidis, I. Poulios, S. Sotiropoulos, *J. Hazard. Mater.* **2012**, *211–212*, 30–46.
[38] J. Georgieva, S. Armyanov, I. Poulios, A. D. Jannakoudakis, S. Sotiropoulos, *Electrochem. Solid-State Lett.* **2010**, *13*, P11–P13.
[39] J. Rongé, S. Deng, S. P. Sree, T. Bosserez, S. W. Verbruggen, N. K. Singh, J. Dendooven, M. B. J. Roeffaers, F. Taulelle, M. De Volder, C. Detavernier, J. A. Martens, *RSC Adv.* **2014**, *4*, 29286–29290.
[40] K. Xu, A. Chatzitakis, E. Vollestad, Q. Ruan, J. Tang, T. Norby, *Int. J. Hydrogen Energy* **2019**, *44*, 587–593.
[41] J. M. Spurgeon, N. S. Lewis, *Energy Environ. Sci.* **2011**, *4*, 2993–2998.
[42] S. Kumari, R. Turner White, B. Kumar, J. M. Spurgeon, *Energy Environ. Sci.* **2016**, *9*, 1725–1733.
[43] J. I. Guo, Y. C. Zhang, A. Zavabeti, K. F. Chen, Y. L. Guo, G. P. Hu, X. L. Fan, G. K. Li, *Nat. Commun.* **2022**, *13*, 5046.
[44] K. O. Iwu, A. Galeckas, A. Y. Kuznetsov, T. Norby, *Electrochim. Acta* **2013**, *97*, 320–325.
[45] X. Kang, L. Chaperman, A. Galeckas, S. Ammar, F. Mammeri, T. Norby, A. Chatzitakis, *ACS Appl. Mater. Interfaces* **2021**, *13*, 46875–46885.
[46] T. Suguro, F. Kishimoto, K. Takanabe, *Energy Fuels* **2022**, *36*, 8978–8994.
[47] F. Dionigi, P. C. K. Vesborg, T. Pedersen, O. Hansen, S. Dahl, A. Xiong, K. Maeda, K. Domen, I. Chorkendorff, *Energy Environ. Sci.* **2011**, *4*, 2937–2942.
[48] S. W. Verbruggen, M. Van Hal, T. Bosserez, J. Rongé, B. Hauchecorne, J. A. Martens, S. Lenaerts, *ChemSusChem* **2017**, *10*, 1413–1418.
[49] F. Amano, A. Shintani, K. Tsurui, H. Mukohara, T. Ohno, S. Takenaka, *ACS Energy Lett.* **2019**, *4*, 502–507.
[50] S. S. Yi, B. R. Wulan, J. M. Yan, Q. Jiang, *Adv. Funct. Mater.* **2019**, *29*, 1801902.
[51] L. Liardet, J. E. Katz, J. Luo, M. Grätzel, X. Hu, *J. Mater. Chem. A* **2019**, *7*, 6012–6020.

Manuscript received: November 9, 2023
Revised manuscript received: January 3, 2024
Version of record online: January 31, 2024